Supplementary Information for

Dynamically Reconfigurable Polarization in Elastomeric Semiconductors for Stretchable Chiroptoelectronics

Ngoc Thanh Phuong Vo[1], Tae Uk Nam[1], Min Woo Jeong[1], Kyu Ho Jung[1], Thuy An Nguyen[1], Seon Hoo Park[1], Hye Rin Chang[1], Guorong Ma[2], Xiaodan Gu[2], Tae Il Le[3], Wonjin Choi[4]*, Jin Young Oh[1]**

[1] Department of Chemical Engineering (Integrated Engineering Program), Kyung Hee University, Yongin, Republic of Korea.

[2]School of Polymer Science and Engineering, University of Southern Mississippi, USA.

[3]Department of Materials Science and Engineering, Gachon University, Republic of Korea.

[4]Lawrence Livermore National Laboratory, 7000 East Ave., Livermore, California, USA.

*Corresponding Authors. Email: t2.lee77@gachon.ac.kr, choi21@llnl.gov, jyoh@khu.ac.kr

Table of Contents Summary

Supplementary Notes

Supplementary Note 1. Characteristics of the FETs

The field effect mobility (μ_{FE}) is calculated in saturation regime by fitting the plot of the linear regime of square root of drain current ($\sqrt{I_D}$) versus gate voltage (V_G). The equation follows (S1):

$$\mu_{FE} = \frac{2L}{WC_i}\left(\frac{\partial\sqrt{I_D}}{\partial V_G}\right)^2 \quad \text{(S1)}$$

Where L is the length of the channel, W is width of the channel. C_i is capacitance per unit area of gate dielectric. The values of all parameters with and without tensile strain are shown at Table S1.

Supplementary Note 2. Calculation method for surface energies of the neat DPPT-TT, 3:7 blend film, and neat SEBS elastomer

The surface free energies are calculated using the Owens-Wendt method[1]:

$$\gamma_c = \gamma_c^p + \gamma_c^d \tag{S2}$$

$$(1 + \cos\theta_l)\gamma_l = 2\left(\sqrt{\gamma_l^d \gamma_c^d} + \sqrt{\gamma_l^p \gamma_c^p}\right) \tag{S3}$$

where γ_c, γ_c^p, and γ_c^d are the total surface energy, polar component and dispersive component of surface energy of testing materials, respectively. Where θ_l, γ_l, γ_l^p, and γ_l^d are the contact angle, total surface energy, polar and dispersive component of surface energy of the test liquid, which are water and diiodomethane. $\gamma_{diiodomethane}$ = 50.8 mJ/m^2, γ_{water} = 72.8 mJ/m^2, γ_{water}^d = 21.8 mJ/m^2 and γ_{water}^p = 51 mJ/m^2.

Supplementary Note 3. Morphology and electrical properties comparison between neat DPPT-TT film and spin coated film under compressive strain

The alignment of nanofibers has a significant influence on the mechanical and optical properties of the DPPT-TT-SEBS composite film making unique than the neat DPPT-TT films. Mechanically, when under compressive strain, neat DPPT-TT films develop macroscale wrinkled surfaces under linear strain, whereas the blend films with SEBS exhibit smoother surface morphologies due to the presence of the elastomeric phase (Supplementary Figs. 10, 11). Besides the changes in mechanical properties induced by blending, the composite also exhibits pronounced optical anisotropy, driven by the alignment of nanoconfined DPPT-TT nanofibers within SEBS perpendicular to the direction of uniaxial strain. The brightness of cross-polarized optical microscopy (POM) images of the composite film reached its maximum and minimum at 0° and 45°, respectively, between the uniaxial strain direction and the polarizer, with the brightness difference increasing proportionally to the strain magnitude, confirming that the optical anisotropy originates from the alignment of nanofibers within the films. The compressively strained neat DPPT-TT films without nanofibers do not exhibit optical anisotropy, highlighting the essential role of aligned nanofibers in strain-induced optical anisotropy (Supplementary Fig. 12).

Supplementary Note 4. Electrical performance of compressed blend film

The activation energy for carrier hopping between nanofibers was extracted from Arrhenius plots for both parallel and perpendicular orientations of the current flow relative to the nanofiber alignment. The results reveal that the activation energy (E_A), contact resistance, and Urbach energy, in the parallel direction is significantly lower than in the perpendicular direction, indicating more efficient charge transport along the nanofiber alignment (Supplementary Figs. 17-23). This trend is consistent with the observed differences in field-effect mobility, further confirming the enhanced charge carrier transport when the current flows parallel to the nanofibers. Therefore, understanding the mechanism behind the electrical anisotropy induced by nanofiber alignment provides a foundation for designing stretchable TFTs with high field-effect mobility.

Supplementary Figures

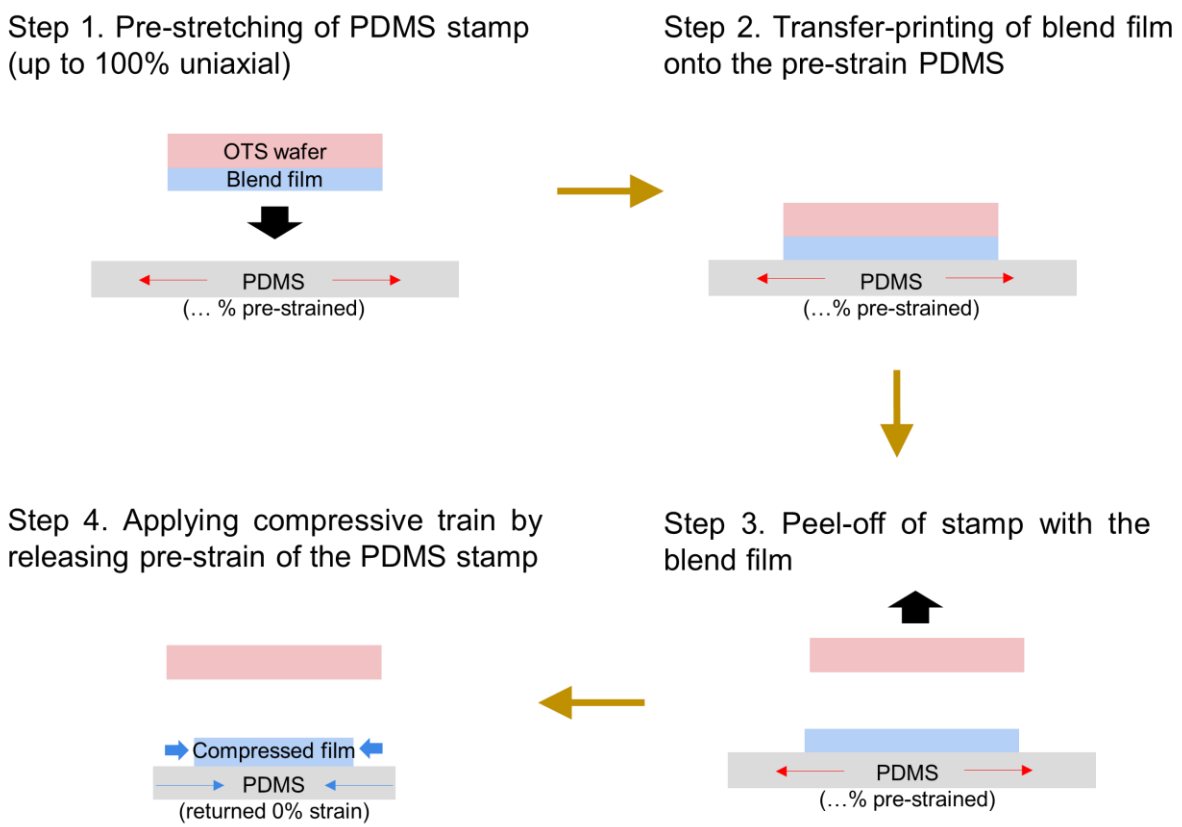

Supplementary Fig. 1. Schematic of the applying of compressive strain to the blend semiconducting film. The degree of the nanofiber alignment is systematically controlled by the pre-strain of PDMS stamp in step 1. The compressive strain is a half of the applied pre-strain.

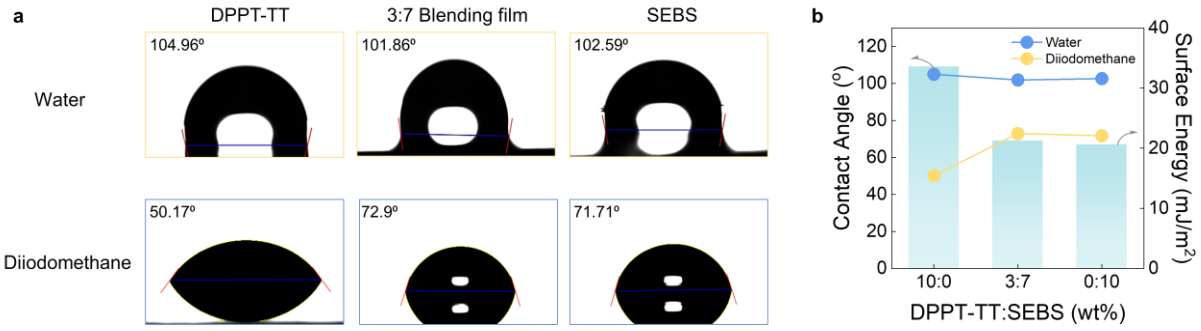

Supplementary Fig. 2. a, Optical images of the contact angles and **b,** surface energies of the neat DPPT-TT, 3:7 blending film and neat elastomer. The surface energies of neat DPPT-TT, DPPT-TT:SEBS (3:7 weight ratio), and neat SEBS are 34.55 mJ/m^2, 22.32 mJ/m^2, 21.7 mJ/m^2, respectively.

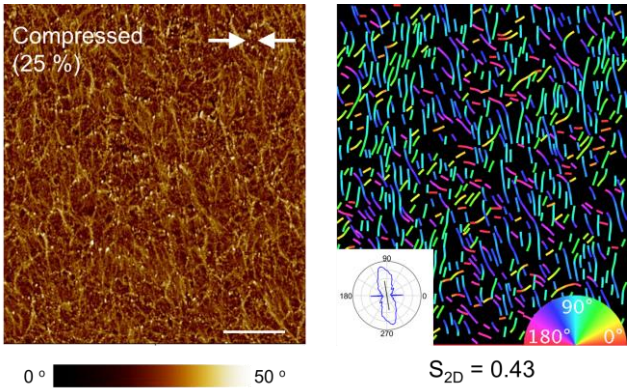

Supplementary Fig. 3. AFM phase images of blend semiconducting films with 25% compressive strain. The white arrows show the compressed direction. The inset (left, bottom) is the orientation distribution and the inset (right, bottom) is the color wheel. The scale bar is 1 μm.

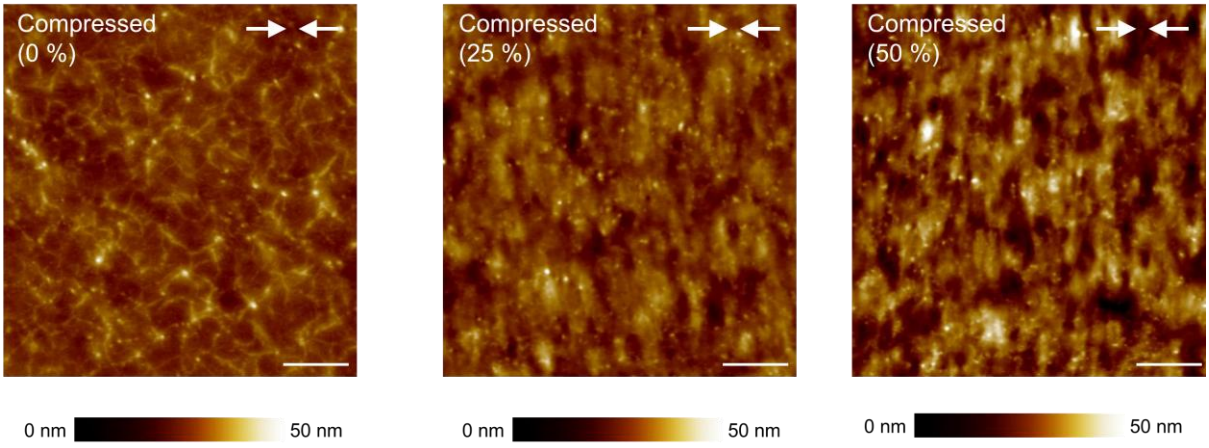

Supplementary Fig. 4. AFM height images of blend semiconducting films with various compressive strain. The white arrows show the compressed direction. The scale bar is 1 μm.

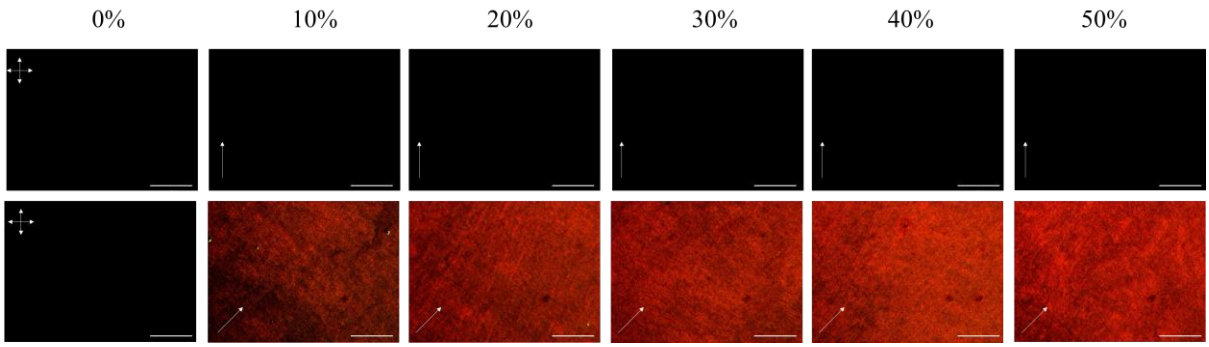

Supplementary Fig. 5. Polarized optical microscopy images of semiconducting films with various compressive strain. The orientation of the cross-polarizers is shown as arrows, and the white arrows indicate the fiber direction. Scale bar: 25 μm.

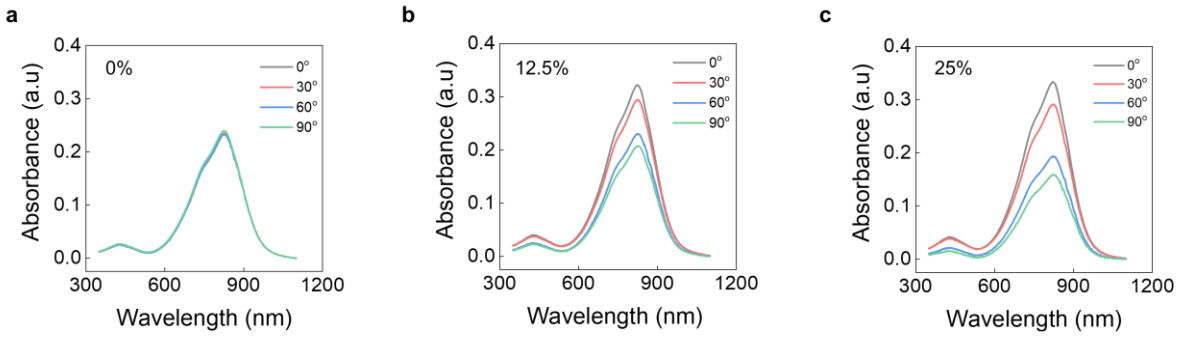

Supplementary Fig. 6. Absorption spectrums of semiconducting films with **a,** 0%, **b,** 12.5%, and **c,** 25% compressive strain.

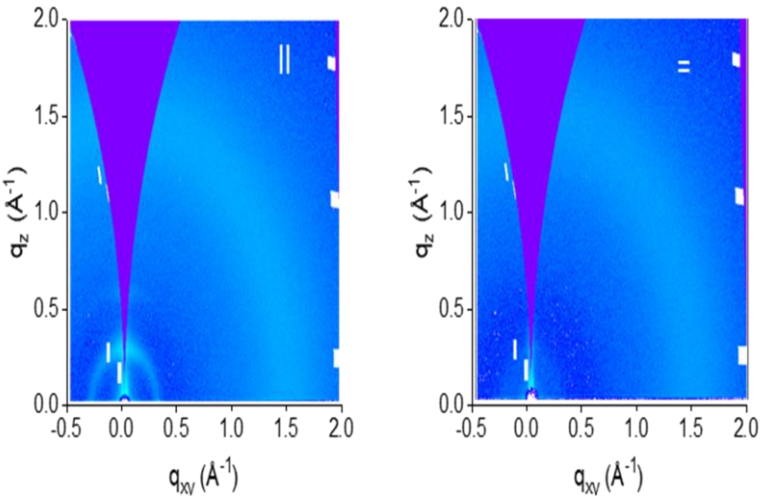

Supplementary Fig. 7. The intensity line cuts for 50 % compressed semiconducting film in out of plane direction, with the incident X-ray beam oriented at different angles with respect to the fiber direction.

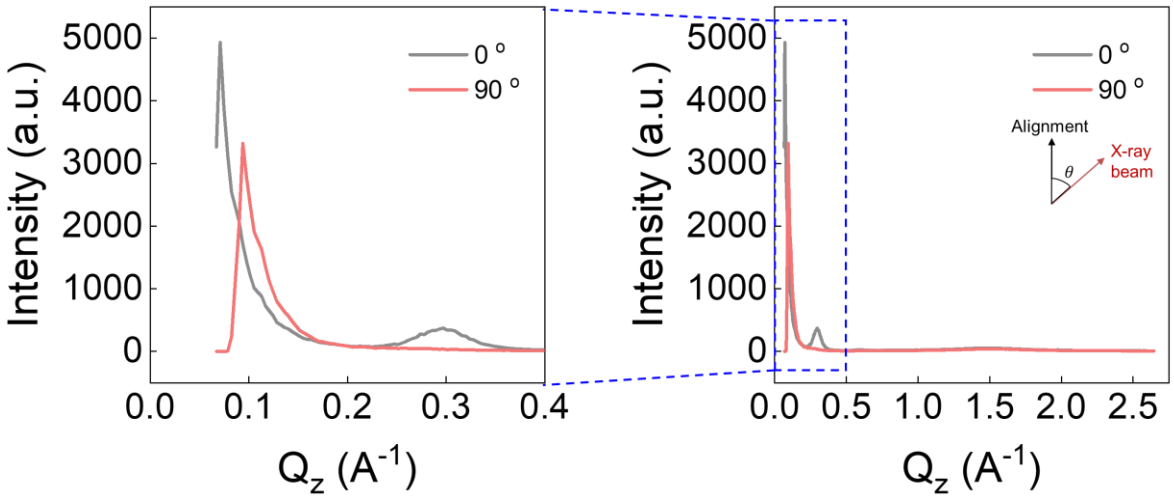

Supplementary Fig. 8. The intensity line cuts for 50 % compressed semiconducting film in out of plane direction, with the incident X-ray beam oriented at different angles with respect to the fiber direction.

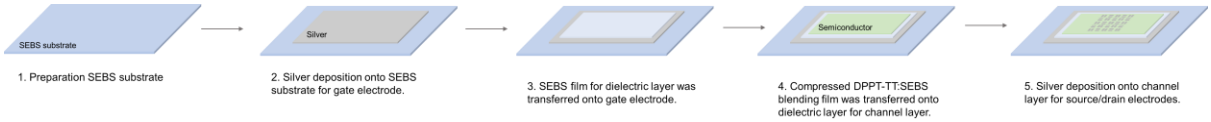

Supplementary Fig. 9. The fabrication process for OTFT device with compressed semiconducting film.

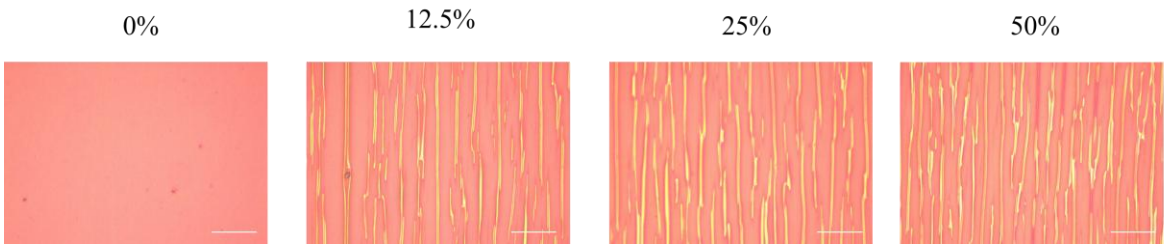

Supplementary Fig. 10. Optical microscopy images of neat semiconducting films with various compressive strain. Scale bar: 25 μm.

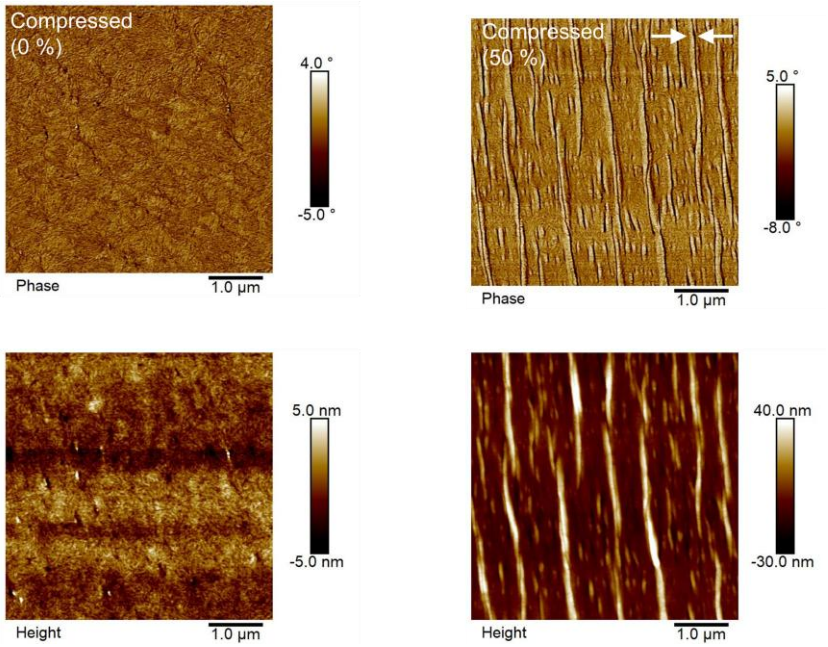

Supplementary Fig. 11. AFM phase (top) and height (bottom) images of neat semiconducting films with various compressive strain. The white arrows show the compressed direction. The scale bar is 1 μm.

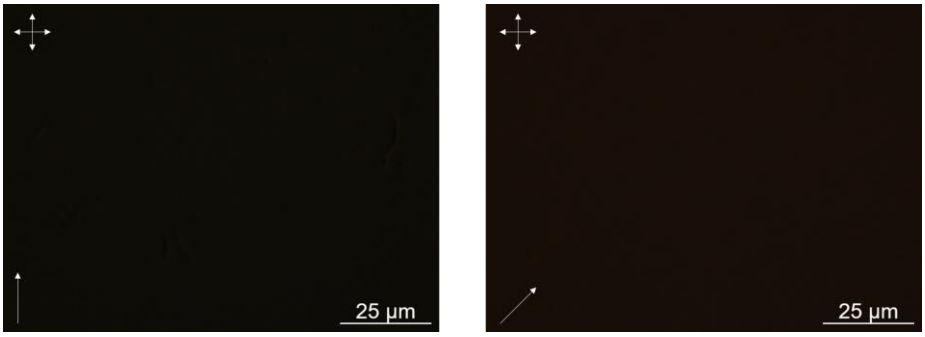

Supplementary Fig. 12. Polarized optical microscopy images of neat DPPT-TT semiconducting films with 50% compressive strain. The orientation of the cross-polarizers is shown as arrows, and the white arrows indicate the wrinkles direction. Scale bar: 25 μm.

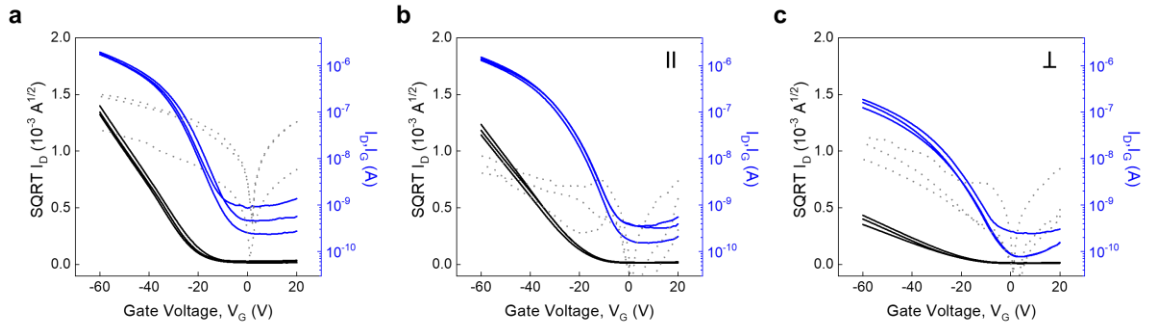

Supplementary Fig. 13. Transfer characteristics of transistor devices with neat DPPT-TT semiconducting layer under **a,** 0% and **b, c,** 50% compressive strain with two directions of compressive train to the channel direction. V_D = -60 V.

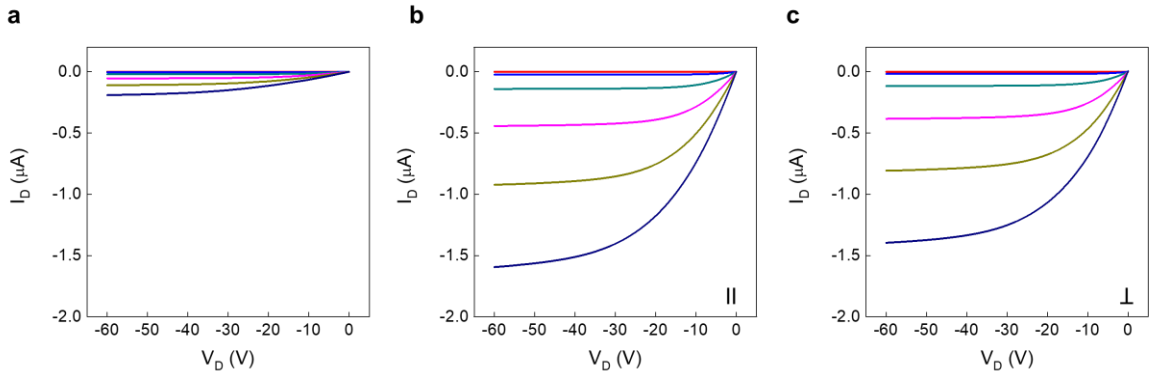

Supplementary Fig. 14. Output characteristics of transistor devices with neat DPPT-TT semiconducting layer under **a,** 0% and **b, c,** 50% compressive strain with two directions of compressive train to the channel direction. V_D = -60 V.

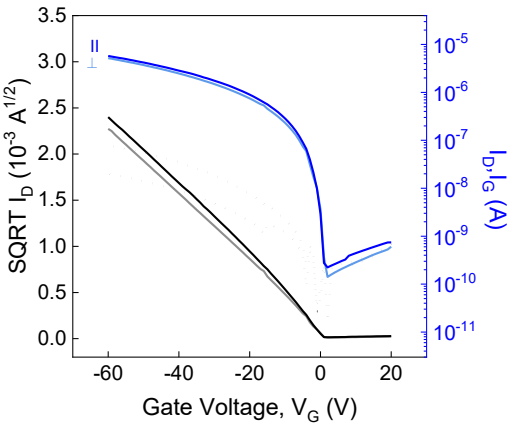

Supplementary Fig. 15. Transfer characteristics of transistor devices with spin coated semiconducting layer in two directions of compressive train to the channel direction. V_D = -60 V.

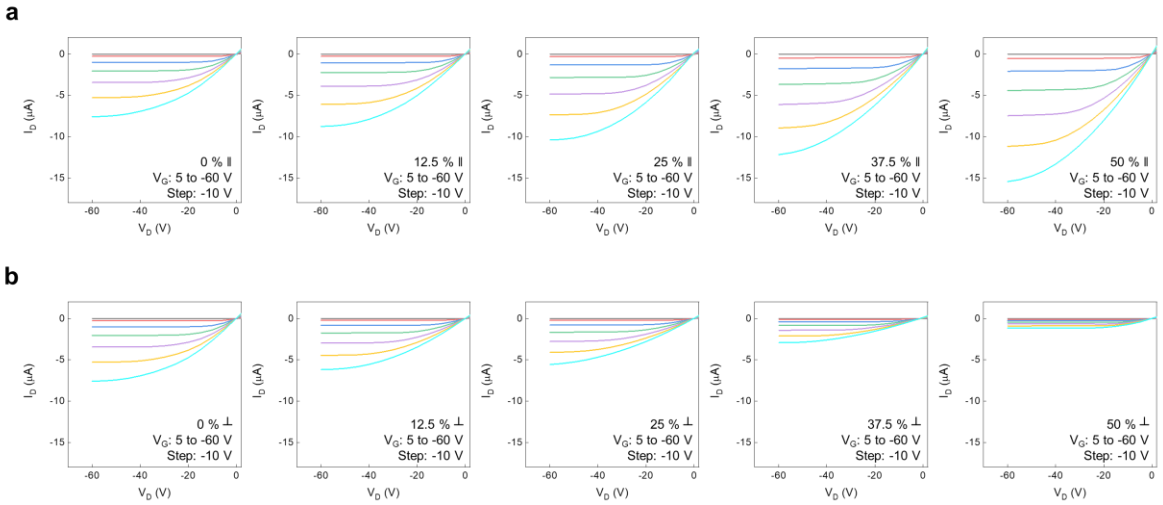

Supplementary Fig. 16. The output characteristics of OTFT devices with blend film under various compressive strain and **a,** parallel and **b,** perpendicular direction between nanofiber alignment and channel. V_D = -60 V.

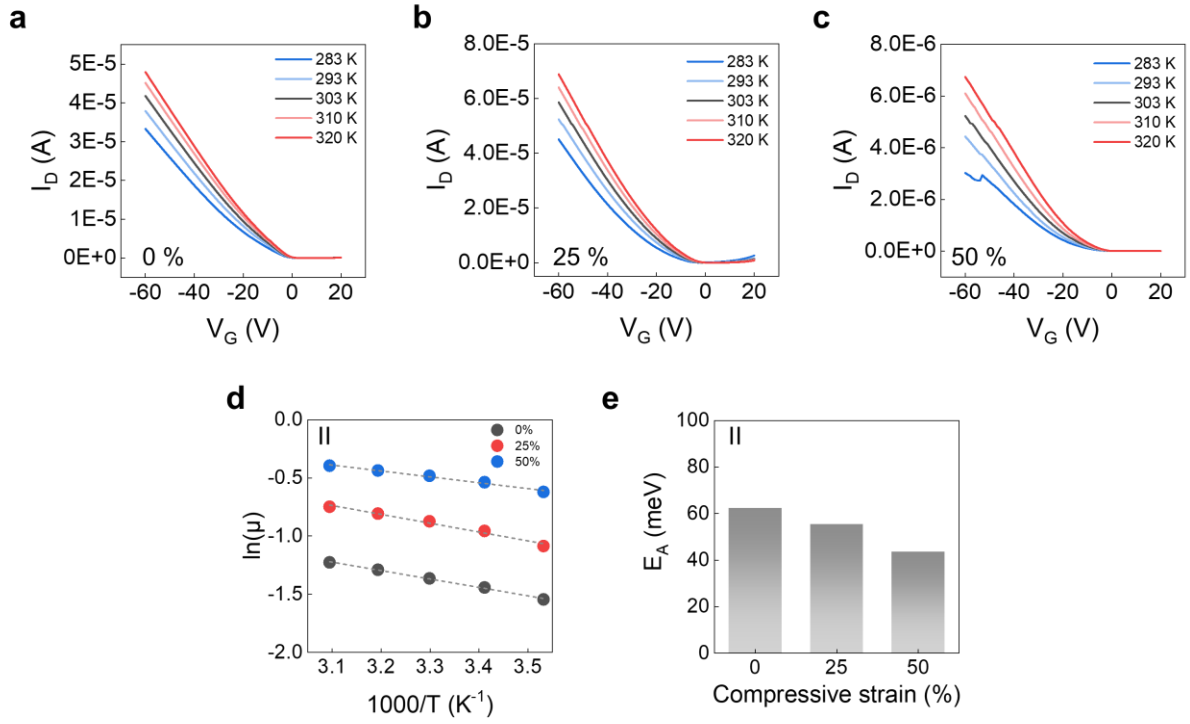

Supplementary Fig. 17. Temperature-dependent transfer characteristics of semiconducting films under **a,** 0 %, **b,** 25 %, and **c,** 50 % compressive strain. The fibers alignment direction is parallel to the channel direction. **d,** Arrhenius plots of the temperature-dependent μ values for different compressed films. The Arrhenius relation: $\mu \propto \exp(-E_A/kT)$, where k is the Boltzmann constant and μ values were measured in the linear regime under low drain–source voltage. The dashed lines show the linear fits of the data. **e,** The activation energies of these compressed films. V_D = -2 V.

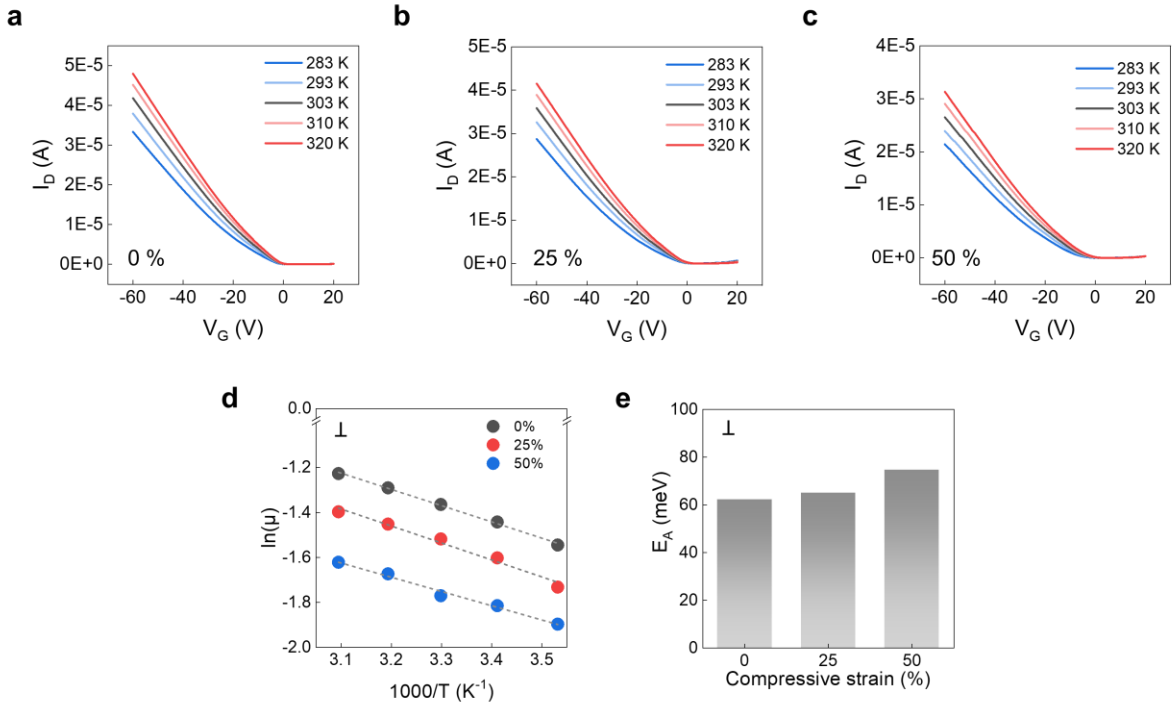

Supplementary Fig. 18. Temperature-dependent transfer characteristics of semiconducting films under **a,** 0 %, **b,** 25 %, and **c,** 50 % compressive strain. The fibers alignment direction is perpendicular to the channel direction. **d,** Arrhenius plots of the temperature-dependent μ values for different compressed films. The dashed lines show the linear fits of the data. **e,** The activation energies of these compressed films. V_D = -2 V.

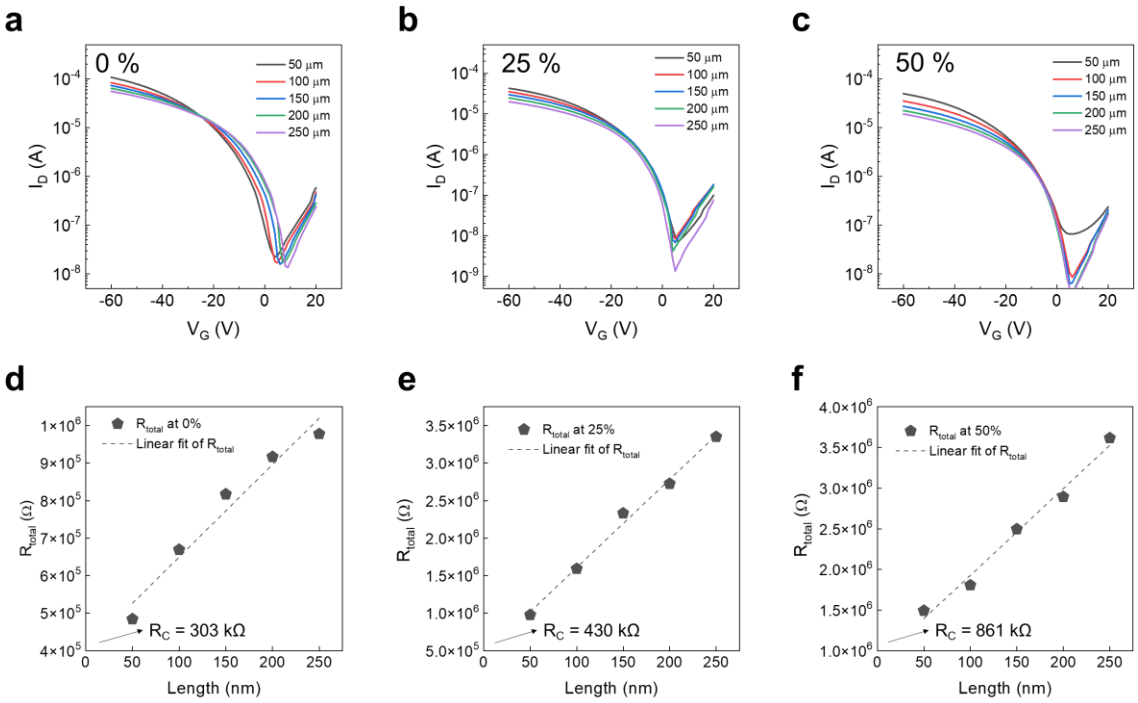

Supplementary Fig. 19. The transfer characteristic of transistor devices with different channel length under **a,** 0 %, **b,** 25 %, and **c,** 50 % compressive strain. The channel direction is perpendicular to the fiber alignment direction. Plots of the total resistance (contact resistance + channel resistance) versus different channel lengths in case of compressive strain induced nanofiber direction parallel to the channel direction at **d,** 0% **e,** 50%, and **f,** 100% compressive strain (channel width, W= 1000 μm). The contact resistance is extracted from the intersection point between Y axis and the fitting line extension at channel length = 0 μm. The drain voltage (V_D) is -30 V.

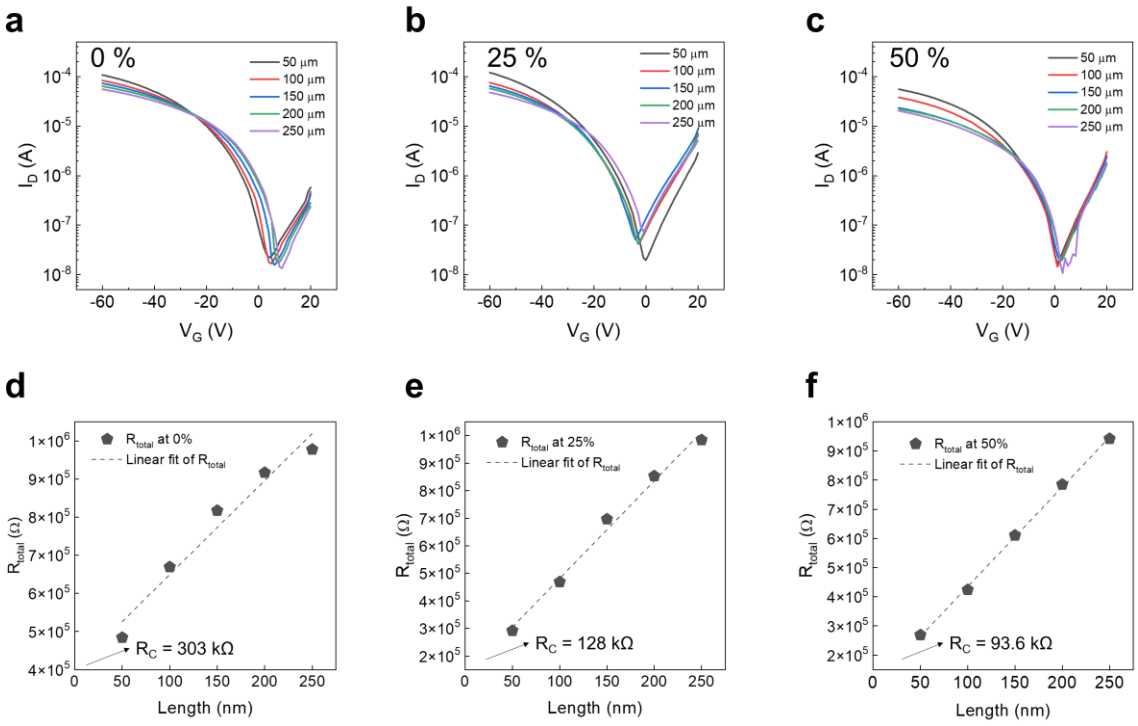

Supplementary Fig. 20. The transfer characteristic of transistor devices with different channel length under **a,** 0 %, **b,** 50 %, and **c,** 100 % compressive strain. The channel direction is parallel to the fiber alignment direction. Plots of the total resistance (contact resistance + channel resistance) versus different channel lengths in case of compressive strain induced nanofiber direction parallel to the channel direction at **d,** 0% **e,** 50%, and **f,** 100% compressive strain (channel width, W= 1000 µm). The contact resistance is extracted from the intersection point between Y axis and the fitting line extension at channel length = 0 μm. The drain voltage (V_D) is -30 V.

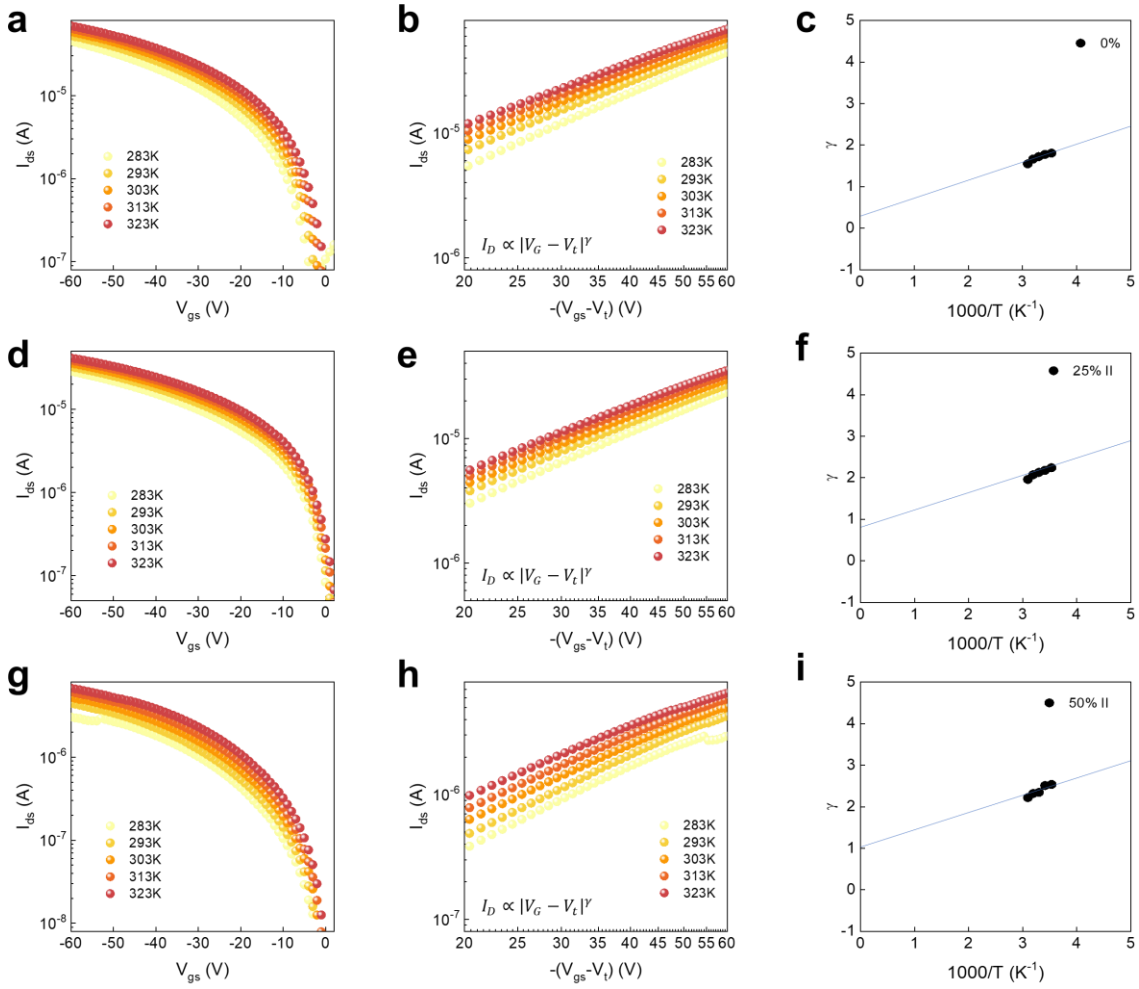

Supplementary Fig. 21. Experimental transfer characteristics of OTFTs (L = 150 μm, W = 1000 μm) as a function of temperature lengths in case of compressive strain induced nanofiber direction perpendicular to the channel direction at **a,** 0 %, **d,** 25 %, and **g,** 50 % compressive strain. Solid lines are fits to equation: $I_D^{2D} = A\frac{W}{L}d_{sc}^{1-(T_0/T)}\left(\frac{C_i}{e}\right)^{T_0/T}\frac{T}{T_0+T}(V_G - V_t)^{(T_0/T)+1}$. **b, e, h,** Replotted transfer characteristics of (a), (d), (g) on a double logarithmic scale. Solid lines are fits to extract the parameter γ for each temperature. **c, f, i,** Extracted values of γ from (b), (e), (h) plotted versus 1/T. The extrapolated dashed linear fit yields the intersection with the vertical axis while the value of T_0 is derived from the slope.

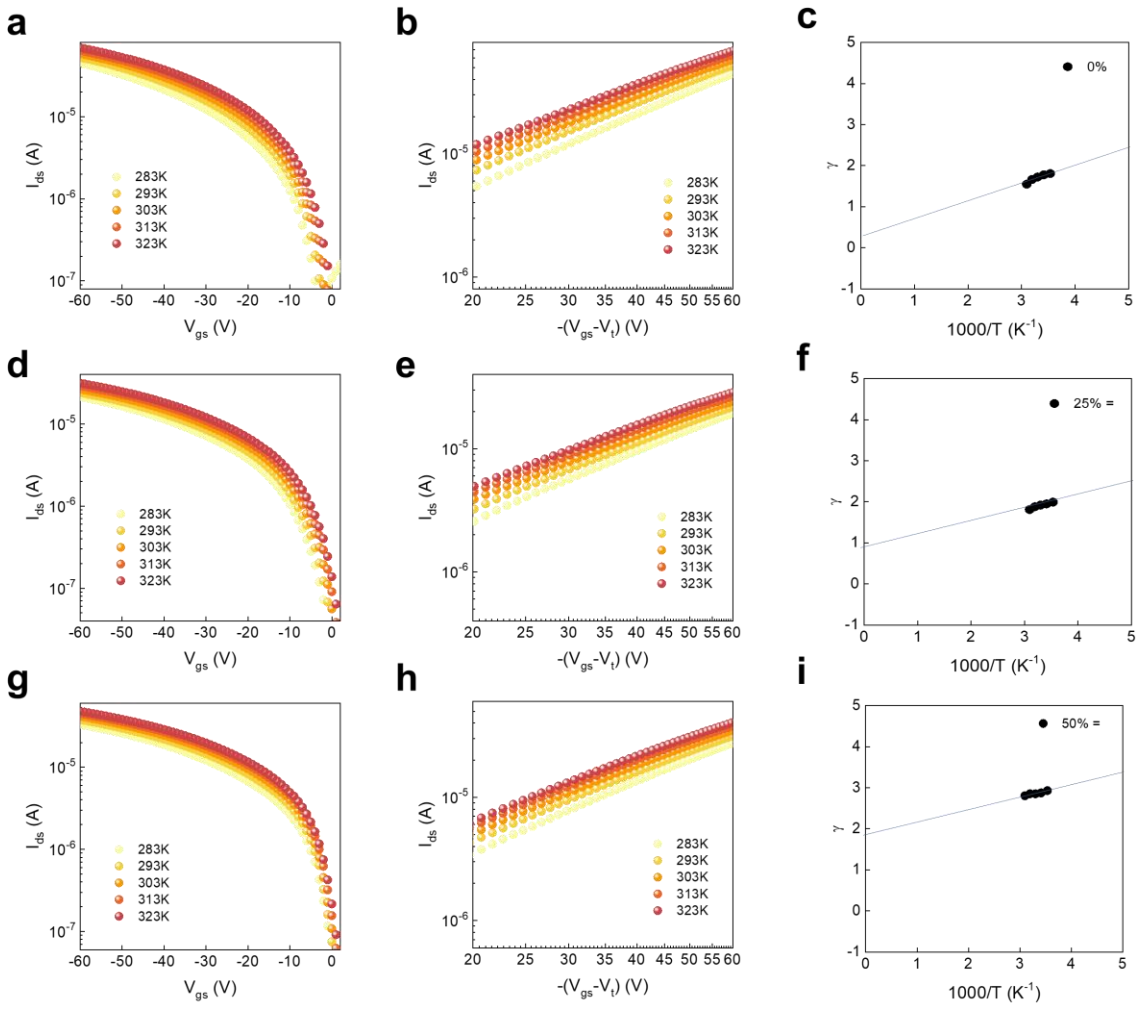

Supplementary Fig. 22. Experimental transfer characteristics of OTFTs (L = 150 μm, W = 1000 μm) as a function of temperature lengths in case of compressive strain induced nanofiber direction parallel to the channel direction at **a,** 0 %, **d,** 25 %, and **g,** 50 % compressive strain. **b, e, h,** Replotted transfer characteristics of (a), (d), (g) on a double logarithmic scale. Solid lines are fits to extract the parameter γ for each temperature. **c, f, i,** Extracted values of γ from (b), (e), (h) plotted versus 1/T. The extrapolated dashed linear fit yields the intersection with the vertical axis while the value of T_0 is derived from the slope.

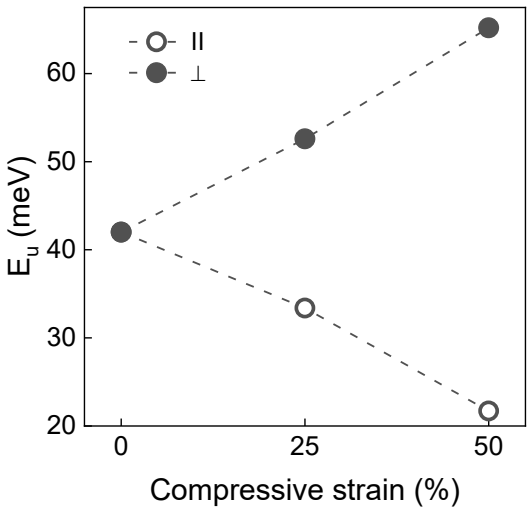

Supplementary Fig. 23. Correlation between the compressive strain and the Urbach energy extracted from the equation (2): $E_u = k_B T_0$ in OTFT transfer characteristics with temperature.

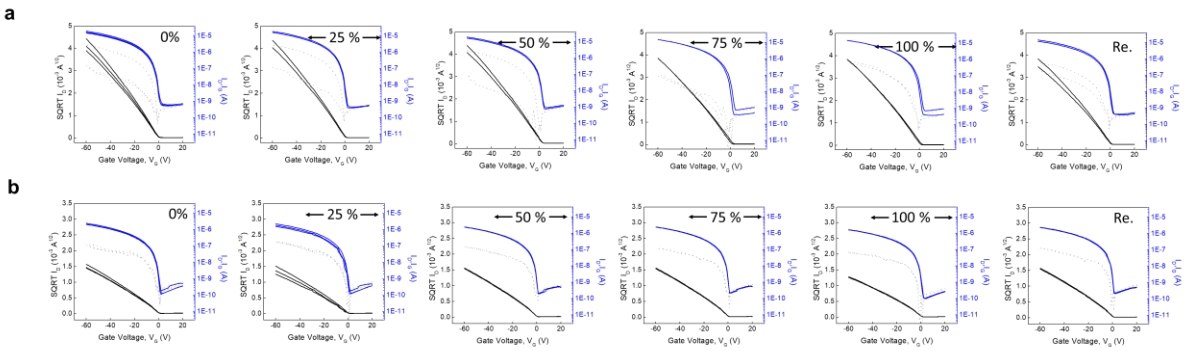

Supplementary Fig. 24. The transfer characteristics of transistor devices with 50 % compressed semiconducting layer under various tensile strain with the a, parallel and b, perpendicular direction of tensile strain to the channel direction (V_D, V_G = -60 V).

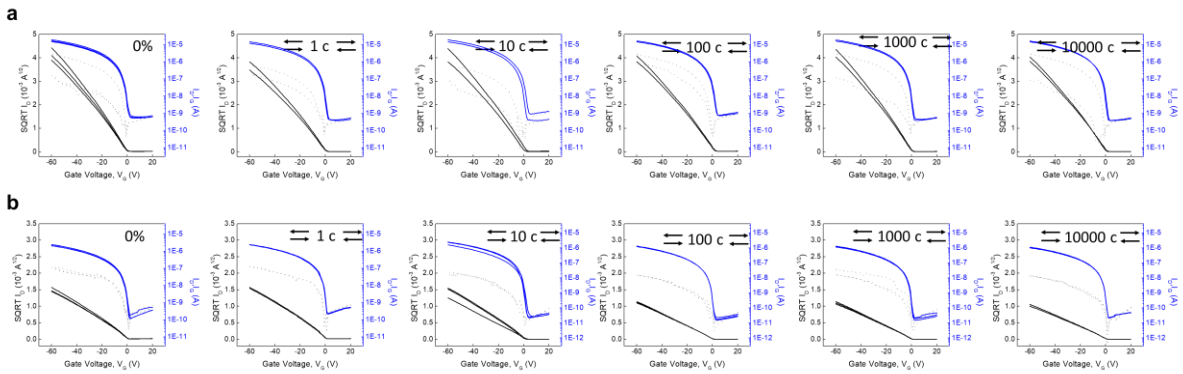

Supplementary Fig. 25. The transfer characteristics of transistor devices with 50 % compressed semiconducting layer under various stretching cycles with **a,** parallel and **b,** perpendicular direction of tensile strain to the channel direction (V_D, V_G = -60 V).

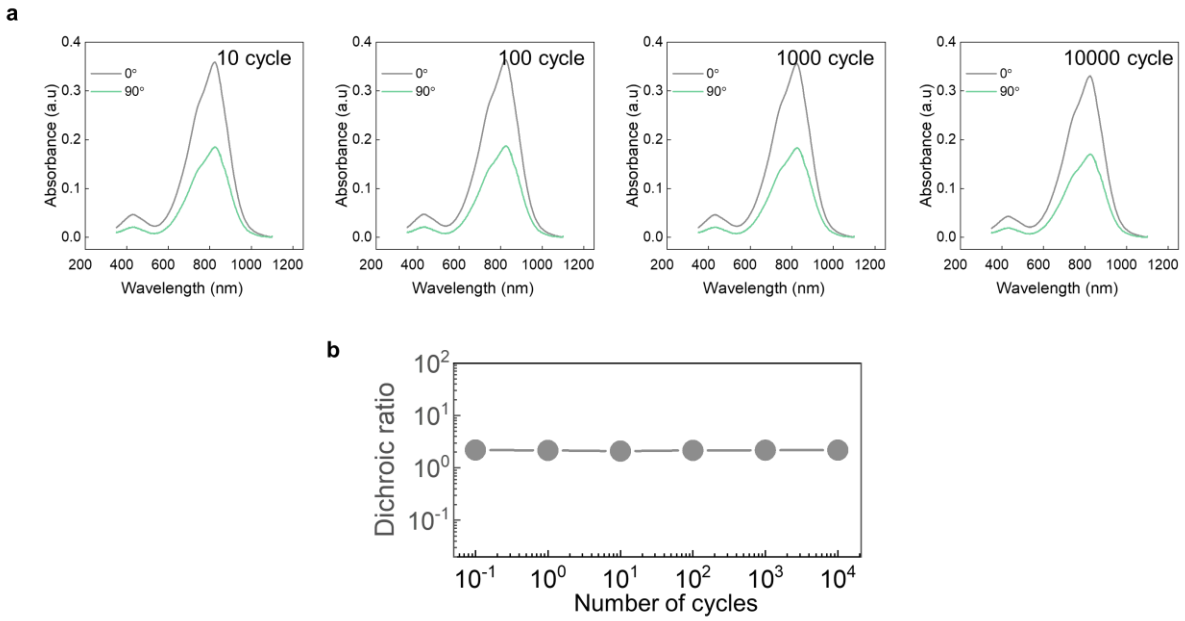

Supplementary Fig. 26. a, The polarized UV-Vis spectra and **b,** dichroic ratio change of 50% compressed film under various cycles of 100% stretching.

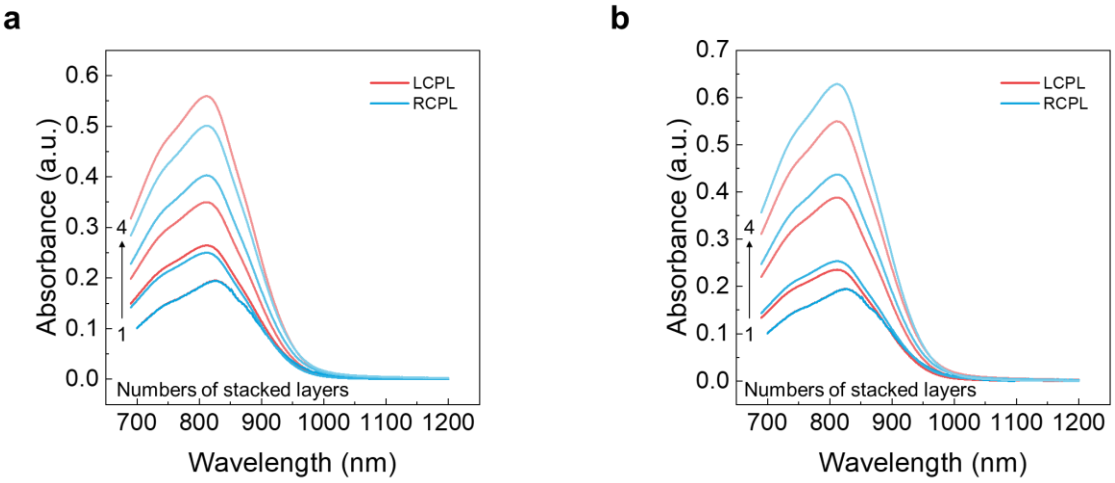

Supplementary Fig. 27. Absorbance spectra with changing numbers of stacked layers of Bouligand structure in **a,** LH and **b,** RH stacked direction.

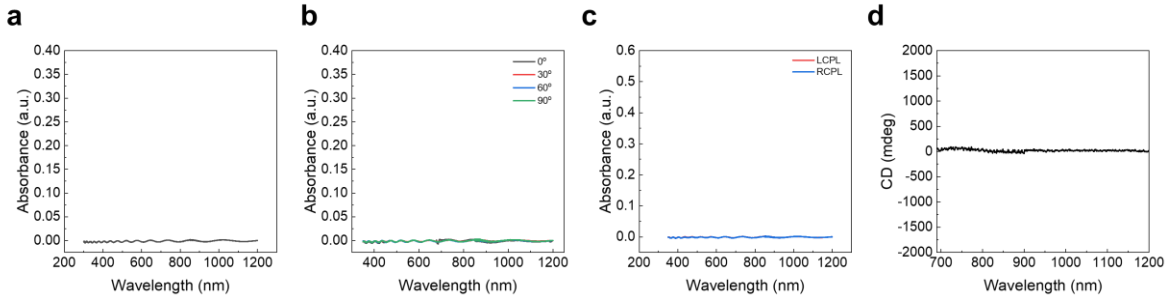

Supplementary Fig. 28. Absorbance spectra under **a,** UV-Vis light, **b,** with linear polarization, and **c,** CPL exposure of pure SEBS films. **d,** The CD spectra of pure SEBS H1062 films under CPL exposure.

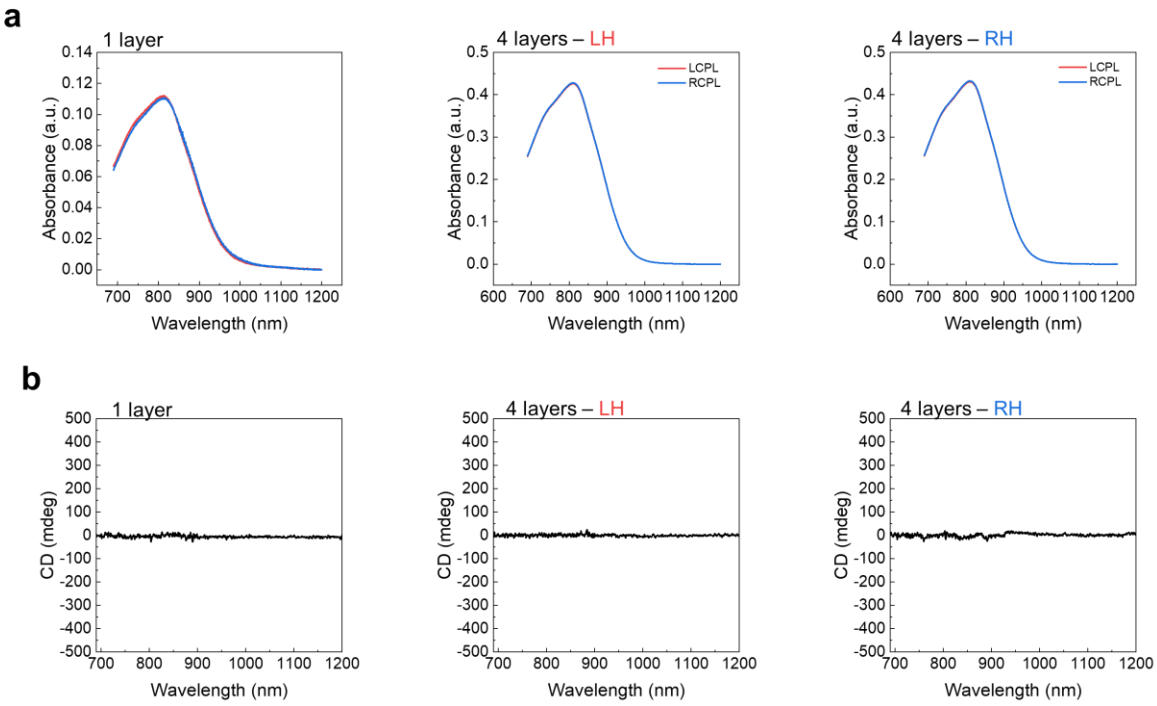

Supplementary Fig. 29. a, Absorbance spectra of stacked neat film under CPL exposure. **b,** The CD spectra of stacked neat films under CPL exposure.

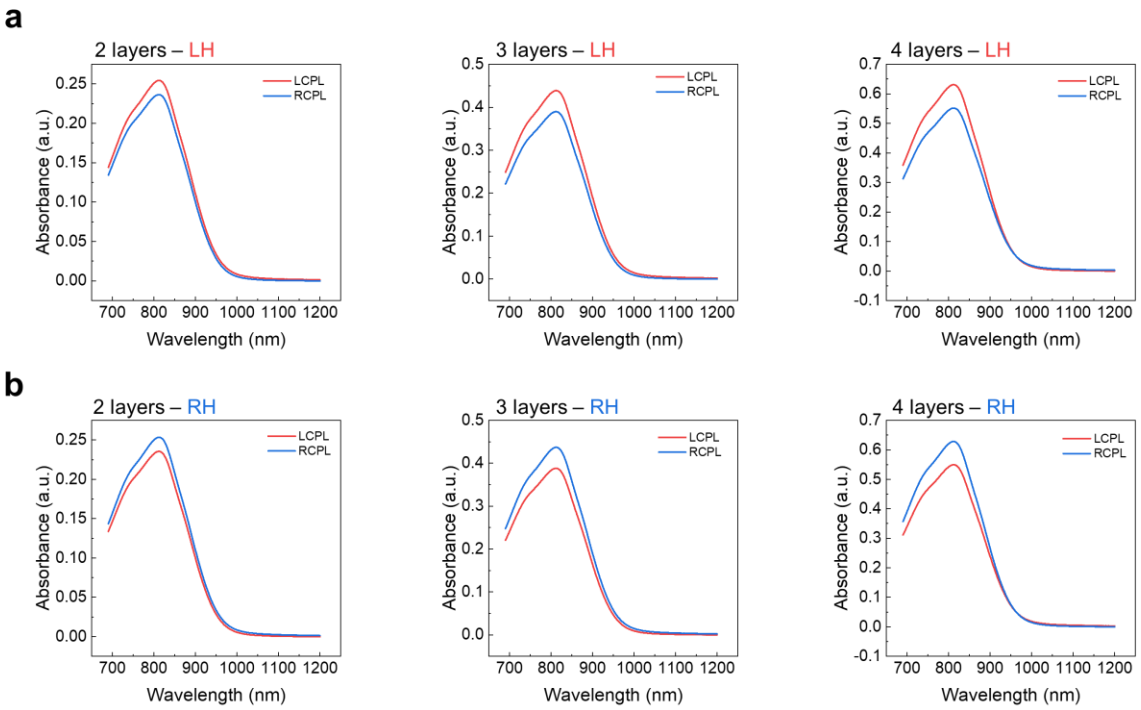

Supplementary Fig. 30. The absorbance spectra of numbers of stacked layers in **a,** LH and **b,** RH direction with 50 % compressive strain and the incident light was exposure in backside of the sample surface.

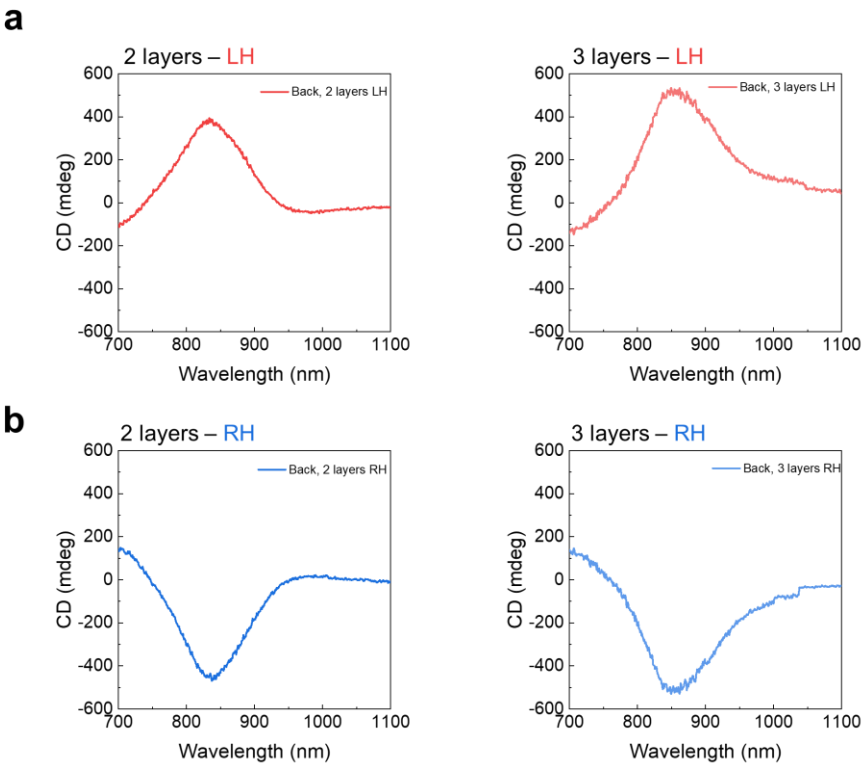

Supplementary Fig. 31. The CD spectra of numbers of stacked layers in **a,** LH and **b,** RH direction with 50 % compressive strain and the incident light was exposure in backside of the sample surface.

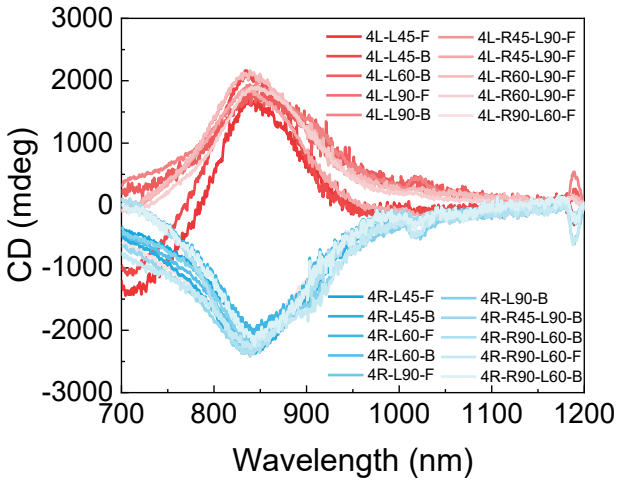

Supplementary Fig. 32. CD spectra with changing incident light, position, and flipping of Bouligand structure.

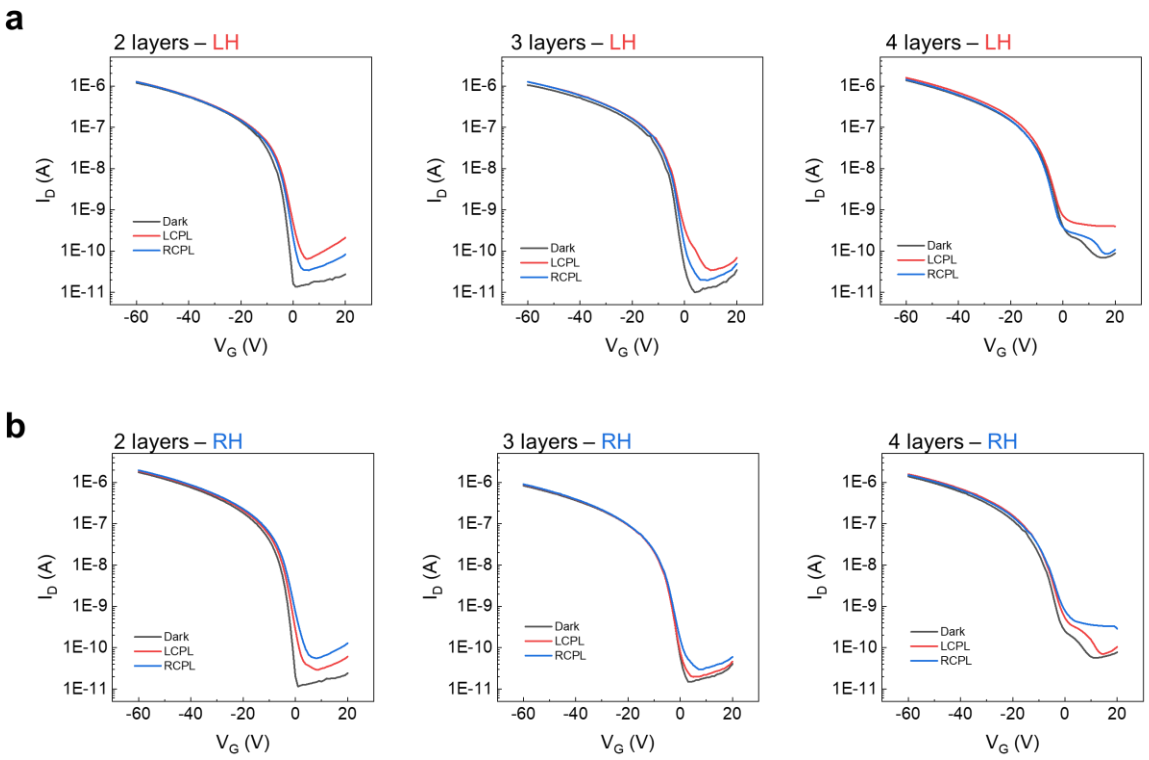

Supplementary Fig. 33. Transfer curves of OTFT devices with changing numbers of stacked layers in **a,** LH and **b,** RH stacked direction. V_D = -60 V.

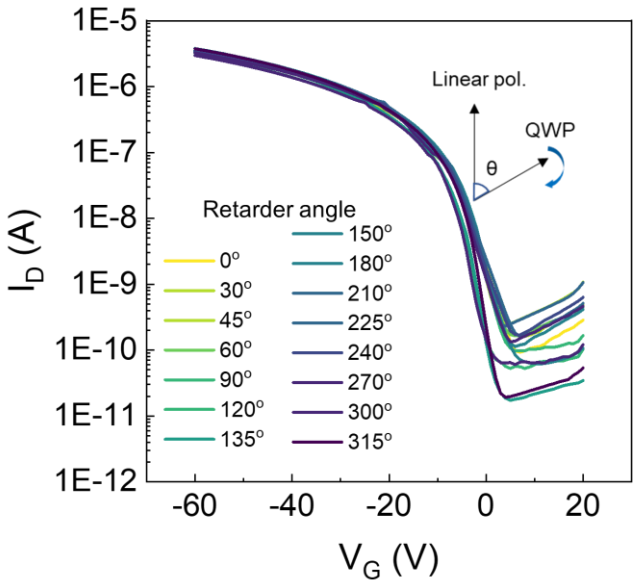

Supplementary Fig. 34. Transfer curves of OTFT devices with Bouligand structure under various retarder angles. V_D = -60 V.

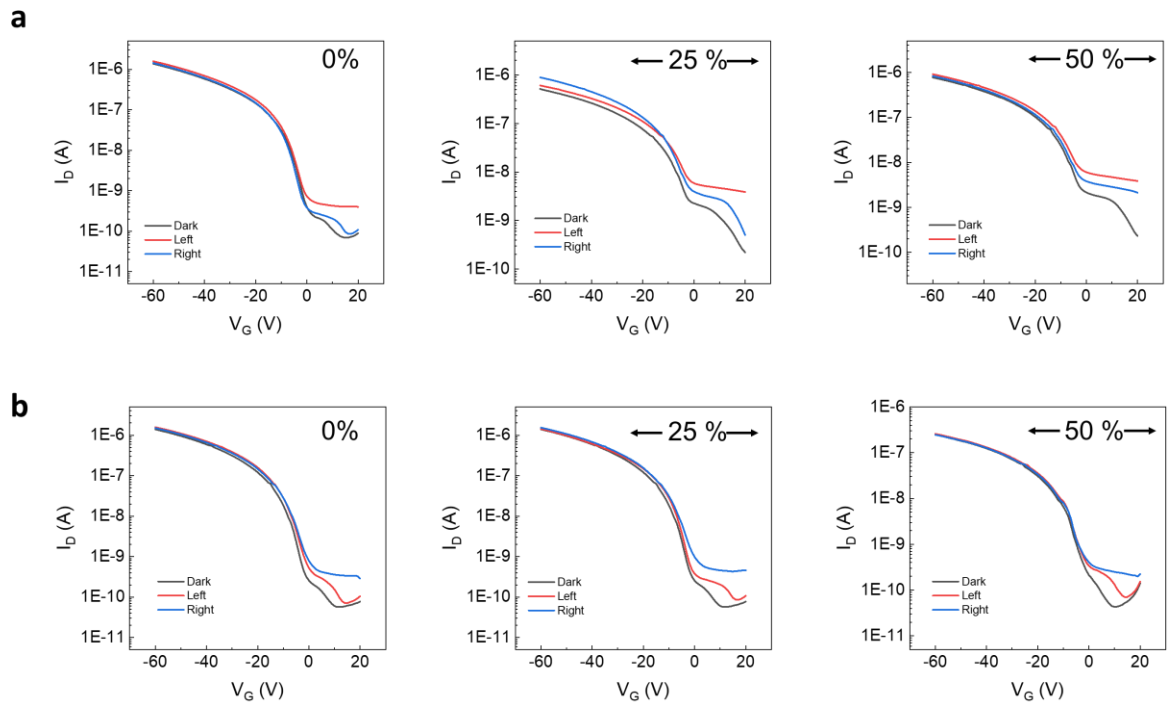

Supplementary Fig. 35. Transfer characteristic of **a,** LH and **b,** RH stacked transistor devices with various uniaxial stretching. V_D = -60 V.

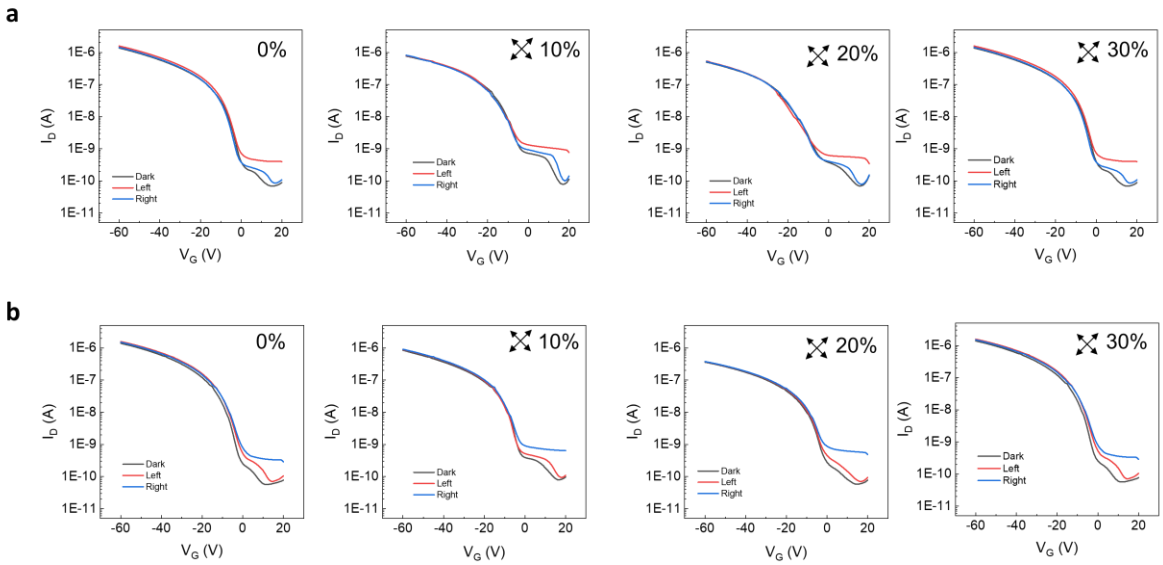

Supplementary Fig. 36. Transfer characteristic of **a,** LH and **b,** RH stacked transistor device with various biaxial stretching. V_D = -60 V.

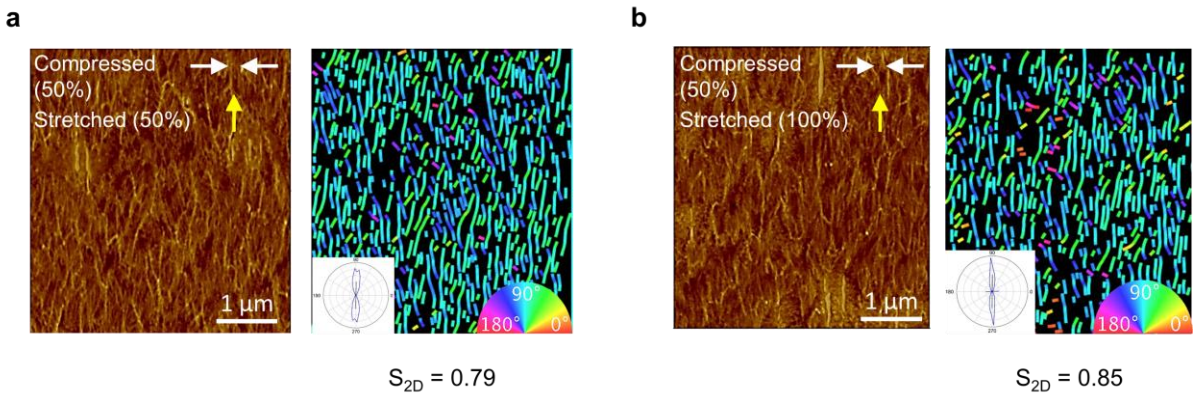

S_{2D} = 0.79 S_{2D} = 0.85

Supplementary Fig. 37. AFM phase images of semiconducting films with 50% compressive strain under **a,** 50% and **b,** 100% parallel tensile strain to nanofiber direction. The white arrows show the compressed direction. The yellow arrows show the stretching direction after compression. The inset (left, bottom) is the orientation distribution and the inset (right, bottom) is the color wheel.

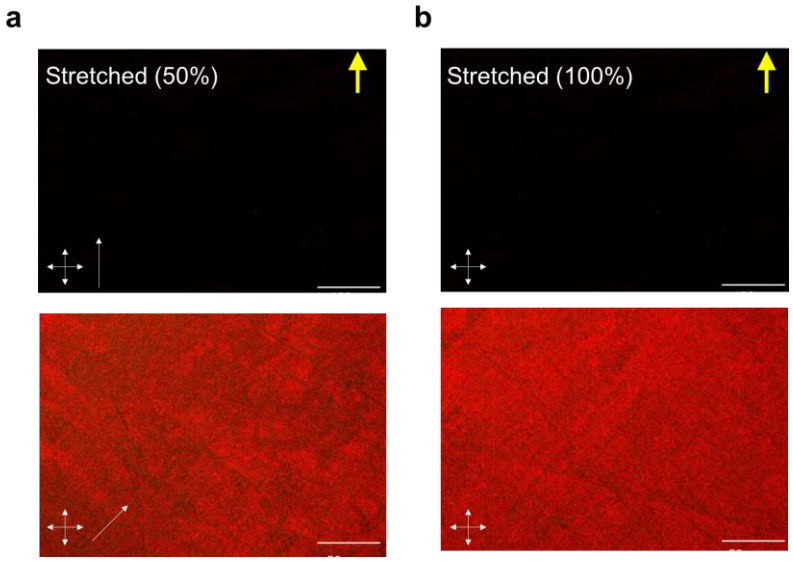

Supplementary Fig. 38. Polarized optical microscopy images of 50% compressed semiconducting films with **a,** 50% and **b,** 100% tensile strain. The orientation of the cross-polarizers is shown as arrows, and the white arrows indicate the fiber direction. The yellow arrows show the stretching direction after compression. Scale bar: 25 μm.

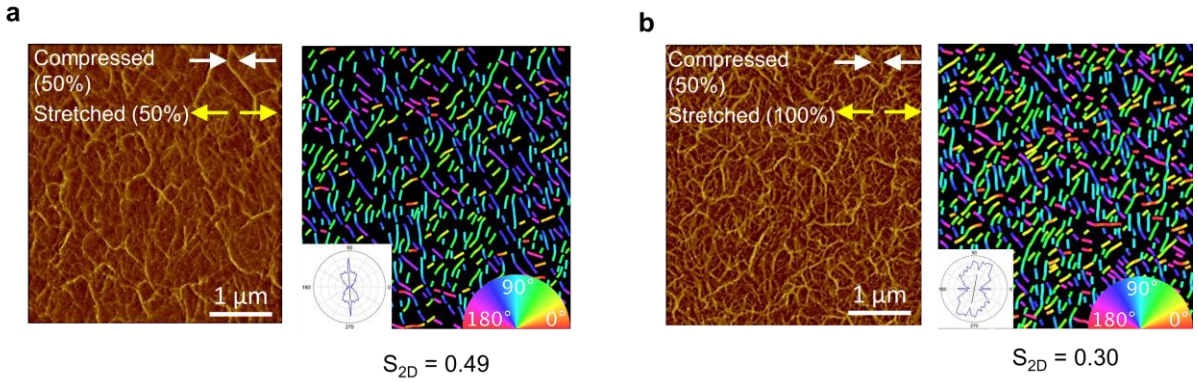

Supplementary Fig. 39. AFM phase images of semiconducting films with 50% compressive strain under **a,** 50% and **b,** 100% perpendicular tensile strain to nanofiber direction. The white arrows show the compressed direction. The yellow arrows show the stretching direction after compression. The inset (left, bottom) is the orientation distribution and the inset (right, bottom) is the color wheel.

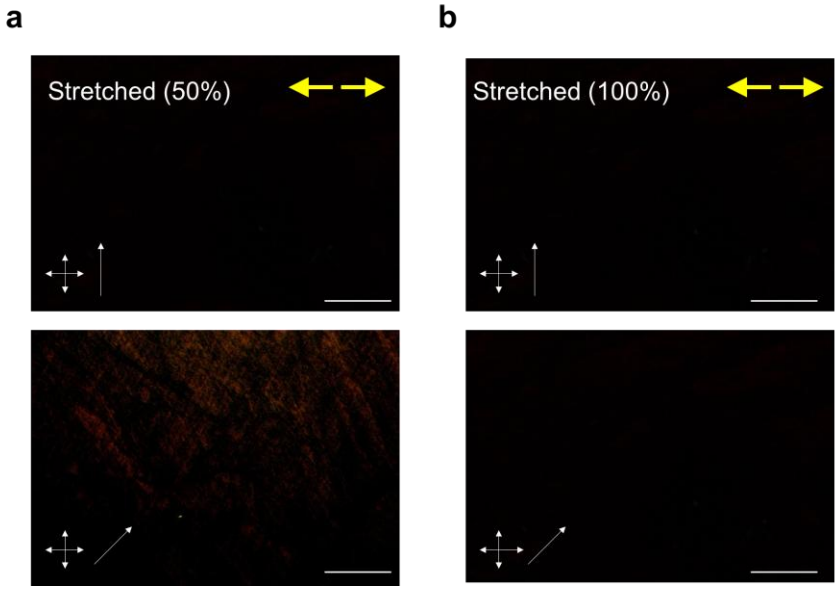

Supplementary Fig. 40. Polarized optical microscopy images of 50% compressed semiconducting films with **a,** 50% and **b,** 100% tensile strain perpendicular to fiber direction. The orientation of the cross-polarizers is shown as arrows, and the white arrows indicate the fiber direction. The yellow arrows show the stretching direction after compression. Scale bar: 25 μm.

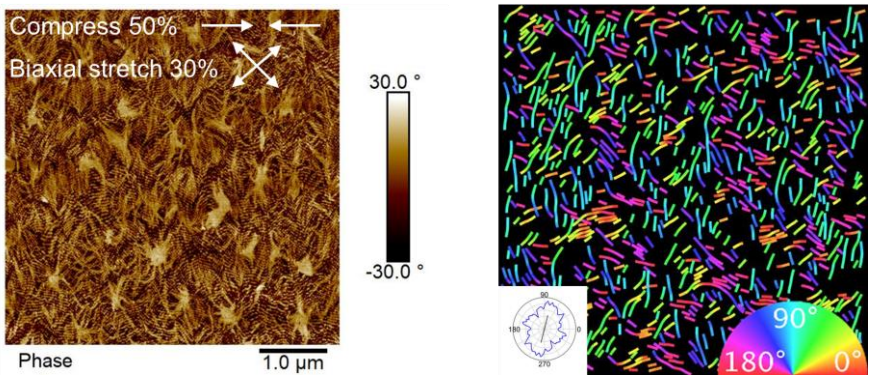

Supplementary Fig. 41. AFM phase images (left) and the fiber direction from GTFiber software (right) of 50 % compressed semiconducting films under 30 % biaxial strain. The white arrows show the compressed direction. The yellow arrows show the lateral stretching direction. The inset (left, bottom) is the orientation distribution and the inset (right, bottom) is the color wheel. The scale bar is 1 μm.

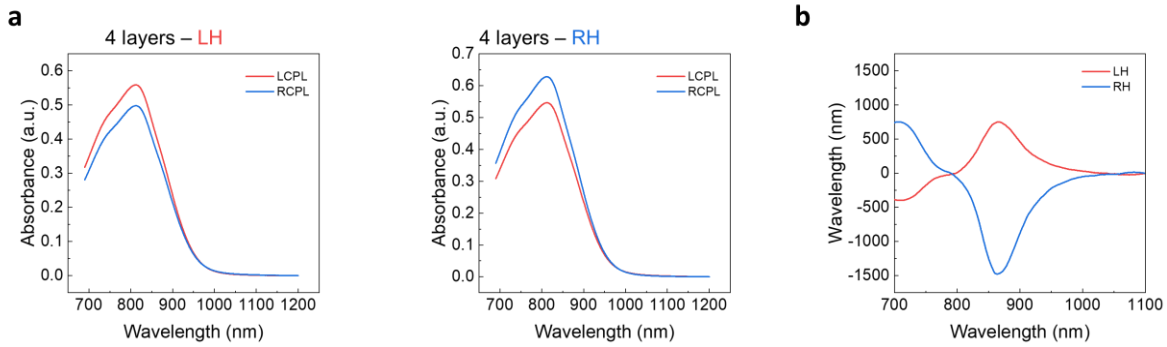

Supplementary Fig. 42. a, UV-Vis absorbance and **b,** CD absorption of 4 stacked layers 25 % uniaxial strain.

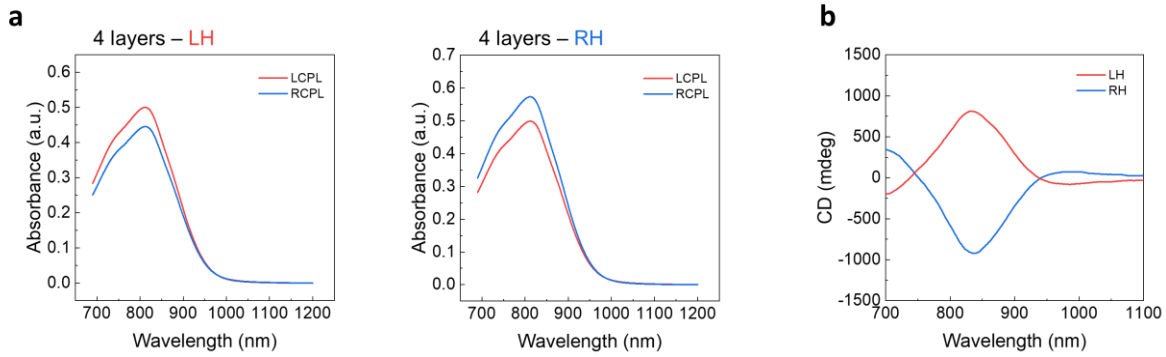

Supplementary Fig. 43. a, UV-Vis absorbance and **b,** CD absorption of 4 stacked layers 50 % uniaxial strain.

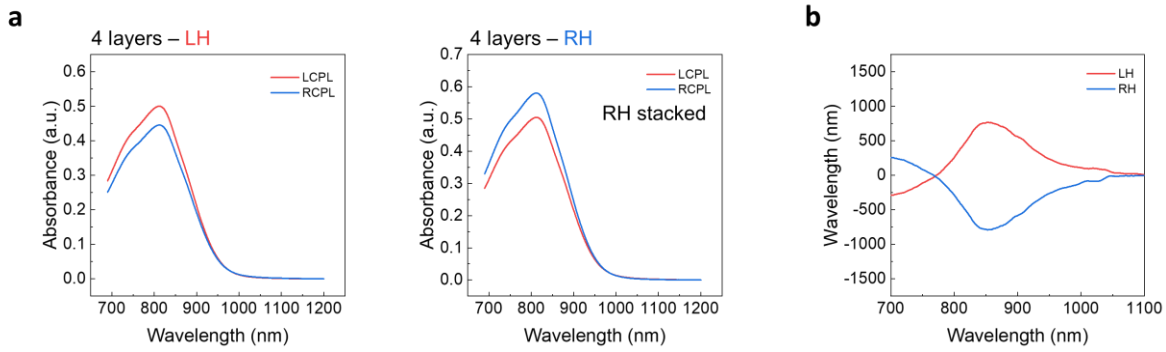

Supplementary Fig. 44. a, UV-Vis absorbance and **b,** CD absorption of 4 stacked layers under 30 % biaxial strain.

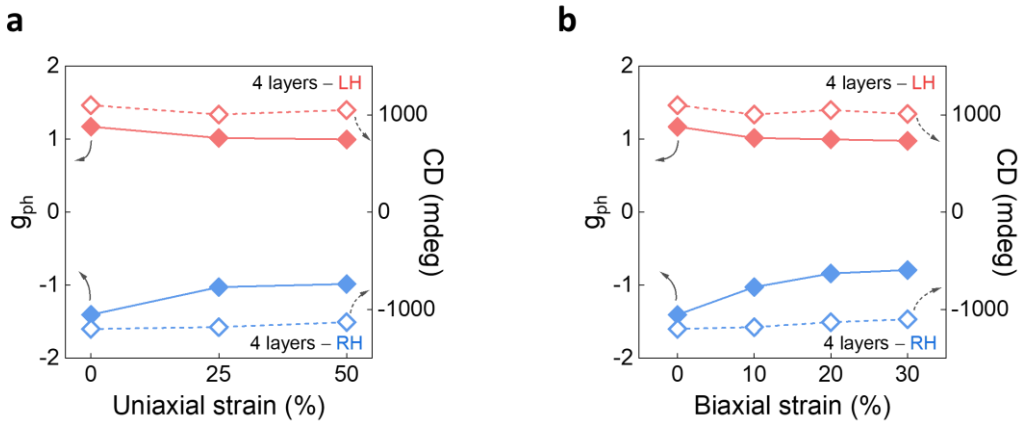

Supplementary Fig. 45. Change of dissymmetry factor and CD response 850 nm under various **a,** uniaxial and **b,** biaxial strain.

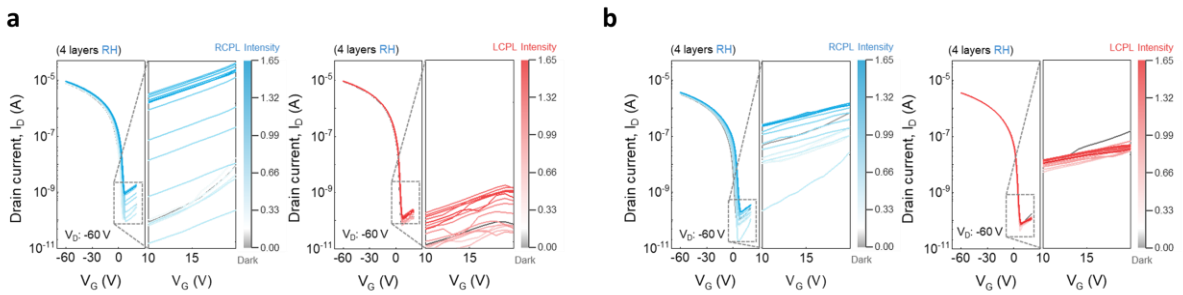

Supplementary Fig. 46. Transfer characteristics of right-handed stacked transistor devices with various laser intensity in **a,** pristine and **b,** biaxial stretching 30% states. V_D = -60 V.

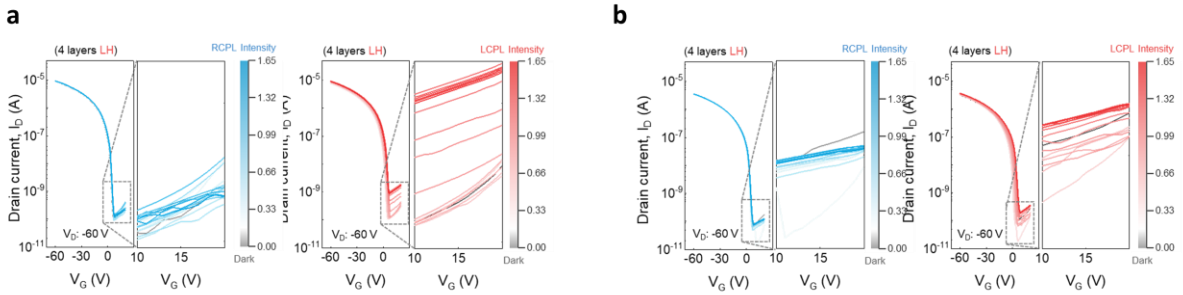

Supplementary Fig. 47. Transfer characteristics of left-handed stacked transistor devices with various laser intensity in **a,** pristine and **b,** biaxial stretching 30% states. V_D = -60 V.

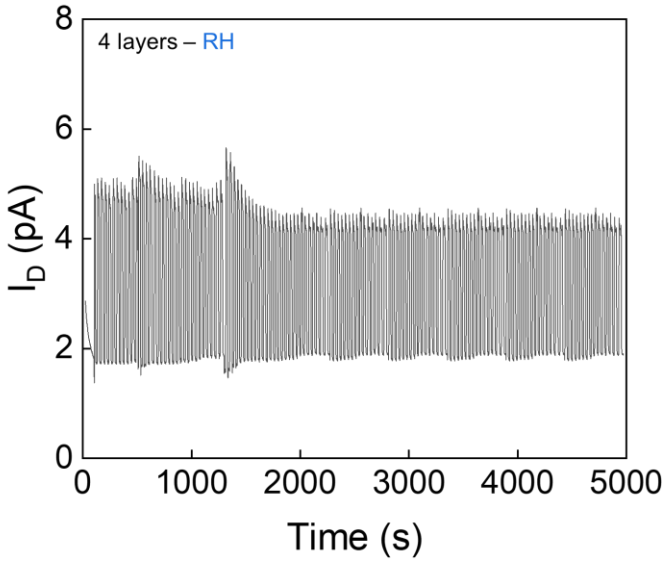

Supplementary Fig. 48. Real time measurement of pristine 4 stacked layers in right-handed direction with sequentially change of LCPL and RCPL. V_D = -10 V, V_G = 0 V.

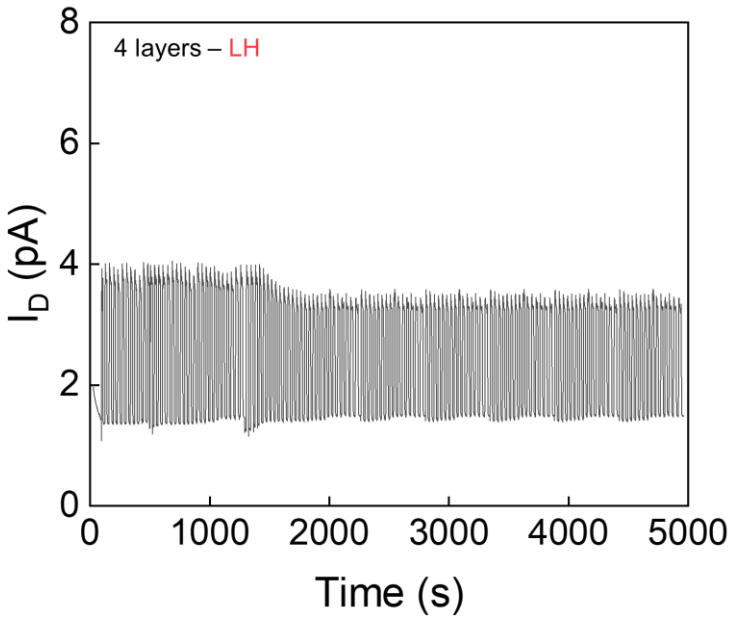

Supplementary Fig. 49. Real time measurement of pristine 4 stacked layers in left-handed direction with sequentially change of LCPL and RCPL. V_D = -10 V, V_G = 0 V.

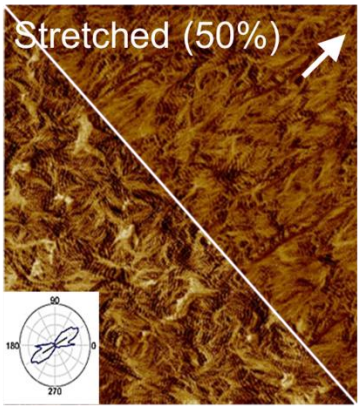

Supplementary Fig. 50. AFM phase images of 2 stacked layers upon stretching with 50% tensile strain. Inset is the orientation map of top layer.

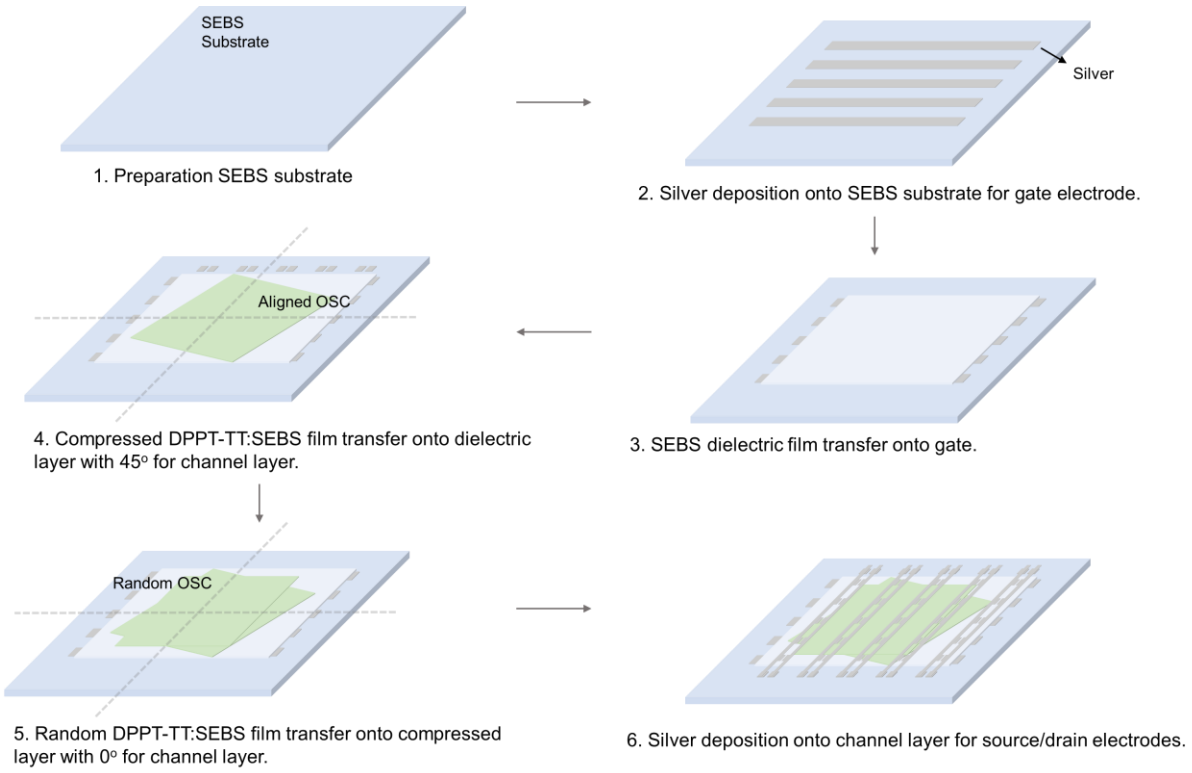

Supplementary Fig. 51. Fabrication steps for stretchable and self-healable active matrix arrays. Silver gate electrode (80 nm) was deposited onto SHE substrate (1.0 μm). SHE dielectric (2.1 μm) and semiconducting film (100 nm) on OTS-treated SiO_2/Si wafer was transferred directly onto silver electrode. Finally, silver S/D electrodes (80 nm) were deposited.

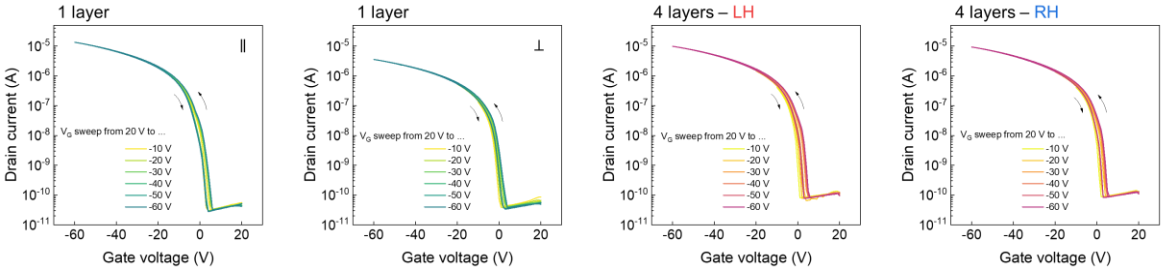

Supplementary Fig. 52. Hysteresis measurements of transistor devices with various gate voltage sweep. V_D = -60 V.

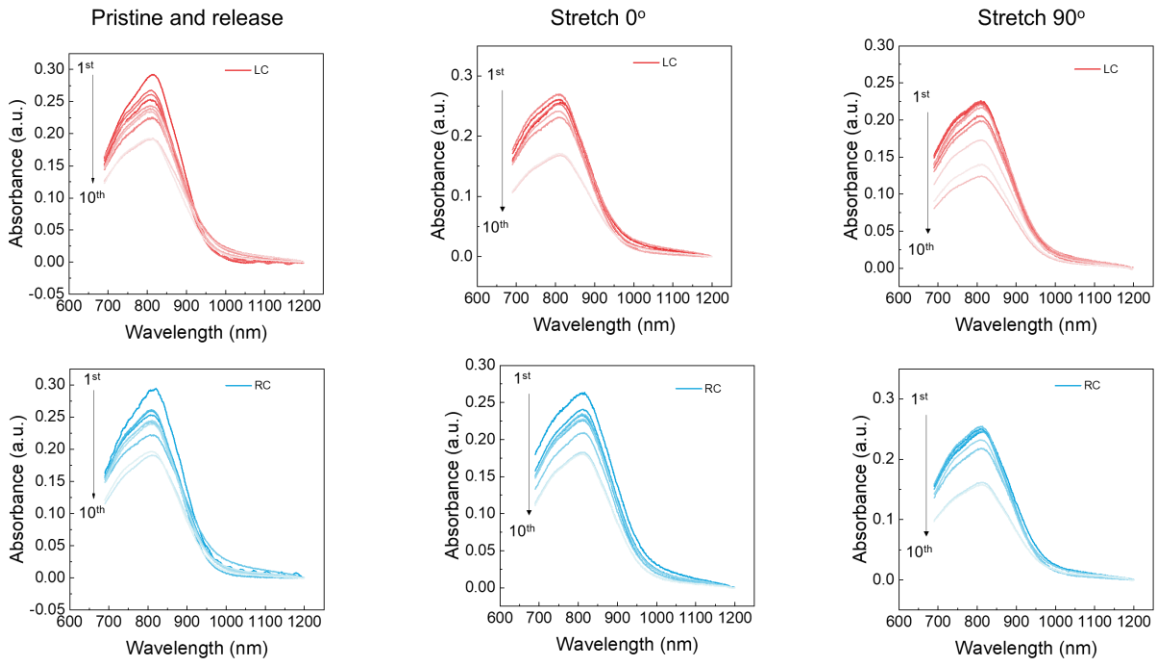

Supplementary Fig. 53. Absorbance of two stacked layer upon stretching 25 % strain up to 10 cycles with different directions of tensile strain.

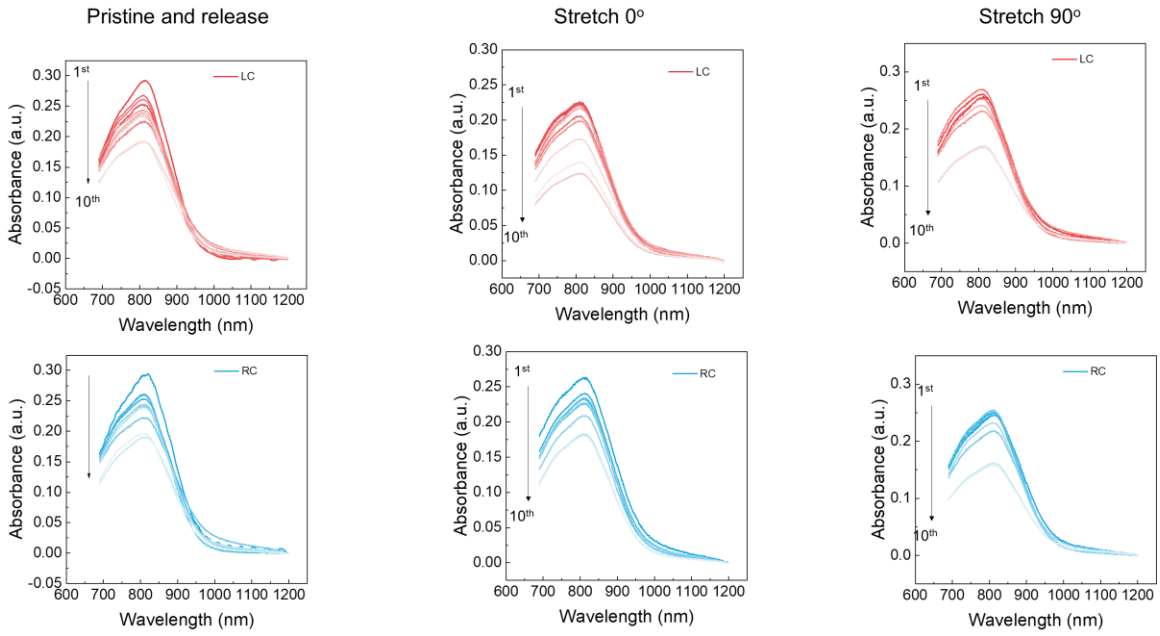

Supplementary Fig. 54. Absorbance of two stacked layer upon stretching 50 % strain up to 10 cycles with different directions of tensile strain.

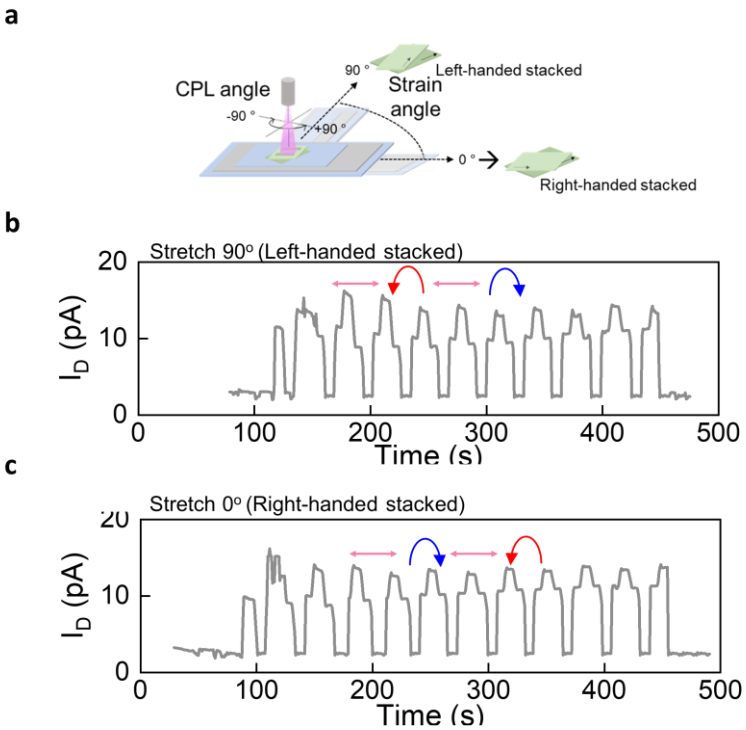

Supplementary Fig. 55. a, Schematic and insitu-real-time measurement of reversible switched **b,** LH and **c,** RH transistor device with changing of quarter wave plate angle. V_G = 0 V, V_D = -10 V.

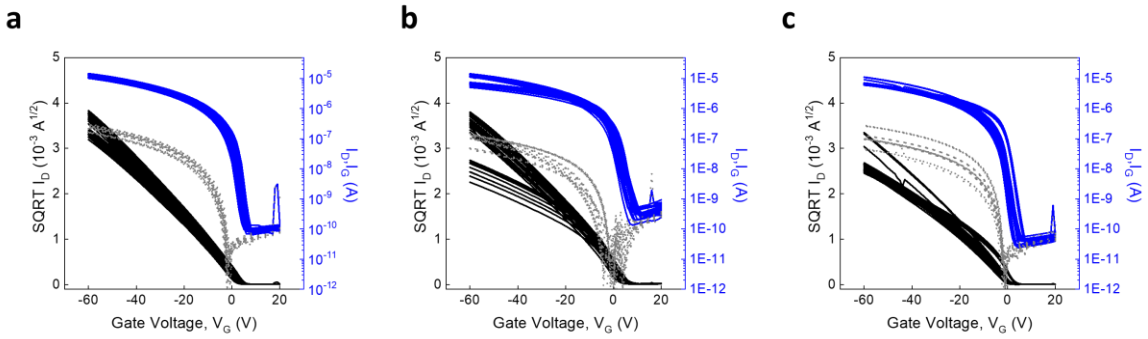

Supplementary Fig. 56. Transfer characteristic of two stacked layers in active-matrix transistor device upon stretching 50 % strain in two directions of tensile strain in 90° under **a,** dark condition, **b,** L-, and **c,** R-CPL exposure. V_D = -60 V.

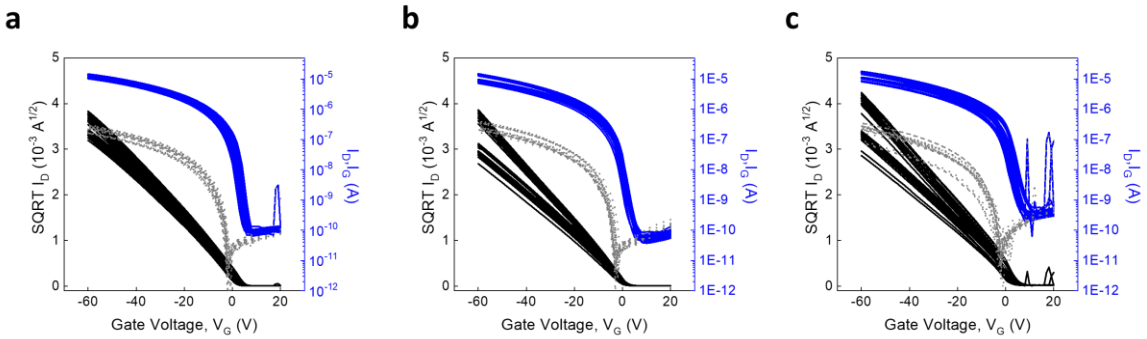

Supplementary Fig. 57. Transfer characteristic of two stacked layers in active-matrix transistor device upon stretching 50 % strain in two directions of tensile strain in 0° under **a,** dark condition, **b,** L-, and **c,** R-CPL exposure. V_D = -60 V.

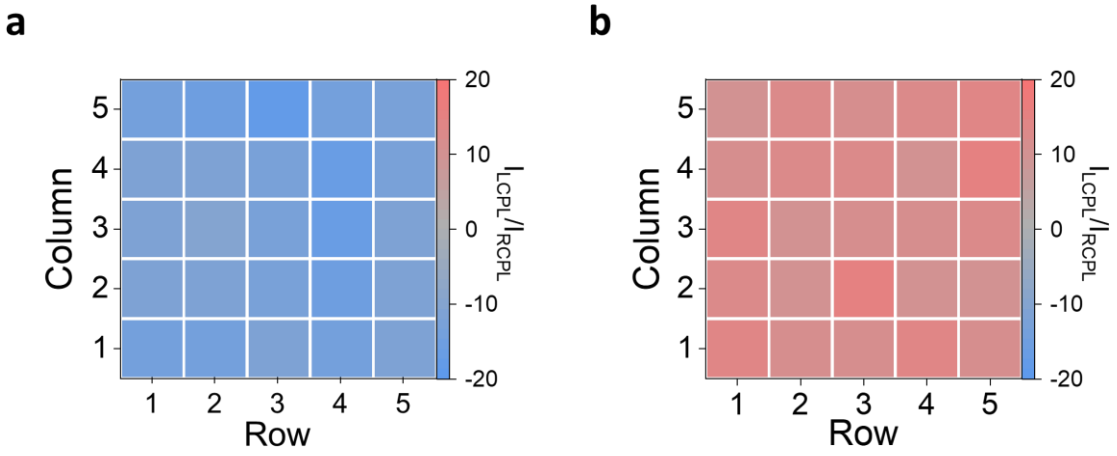

Supplementary Fig. 58. Spatial photocurrent mapping ratio of active-matric array under **a,** 0° and **b,** 90° stretching under CPL exposure.

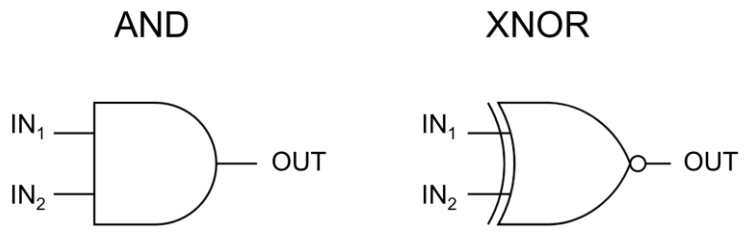

IN_1	IN_2	Out
0	0	0
0	1	0
1	0	0
1	1	1

IN_1	IN_2	Out
0	0	1
0	1	0
1	0	0
1	1	1

Supplementary Fig. 59. Logic table for switchable CPL detector.

Supplementary Table 1. Device geometry and dielectric capacitance under strain.

Stretching	Strain (%)	Channel length (μm)	Channel width (μm)	Capacitance (nF/cm^2)
Uniaxial (ǁ)	0	150	1000	1.75
	10	168	953	1.63
	20	184	932	1.71
	30	198	910	1.82
	40	212	871	1.97
	50	221	865	2.03
	75	228	818	2.12
	100	276	747	2.25
	Release	153	956	1.59
Uniaxial (=)	0	150	1000	1.75
	10	140	1051	1.48
	20	135	1175	1.64
	30	130	1216	1.60
	40	127	1323	1.89
	50	123	1426	2.05
	75	115	1569	2.10
	100	109	1939	2.19
	Release	140.12	1032.02	1.631
Biaxial (×)	0	150	1000	1.75
	10	176	1032	1.89
	20	188	1092	1.95
	30	199	1148	2.21

Note that the capacitance values of gate dielectric were obtained at 1 kHz.

Supplementary Table 2. Linear dynamic range of Bouligand-structured devices with different device states.

Light intensity range (mW/cm²)	**Sensitivity (cm²/mW)**					
Linear dynamic range (0.645-1.504)	**4 layers – LH**			**4 layers – RH**		
	Pristine	*Uniaxial 50%*	*Biaxial 30%*	*Pristine*	*Uniaxial 50%*	*Biaxial 30%*
	31.62	36.43	30.27	27.51	35.87	31.04

Supplementary Table 3. Various input data cases to observe the dynamic switching CPL detection by tuning the angle of stretching and CPL in switchable device.

Strain (On/Off)	Strain (On/Off)	Strain direction (0^o/90^o)	Light direction (RCPL/LCPL)	Output
1	1	1	1	1
1	1	1	0	0
1	1	0	1	0
1	1	0	0	1
1	0	1	1	0
1	0	1	0	0
1	0	0	1	0
1	0	0	0	0
0	1	1	1	0
0	1	1	0	0
0	1	0	1	0
0	1	0	0	0
0	0	1	1	0
0	0	1	0	0
0	0	0	1	0
0	0	0	0	0

Reference

1. Owens, D. K. et al. Estimation of the surface free energy of polymers. *J. Appl. Polym. Sci.* **13**, 1741–1747 (1969).